Characterization and Application of Nanomaterials

VOLUME 2 , ISSUE 2 , 2019

2

ISSN: 2578-1995

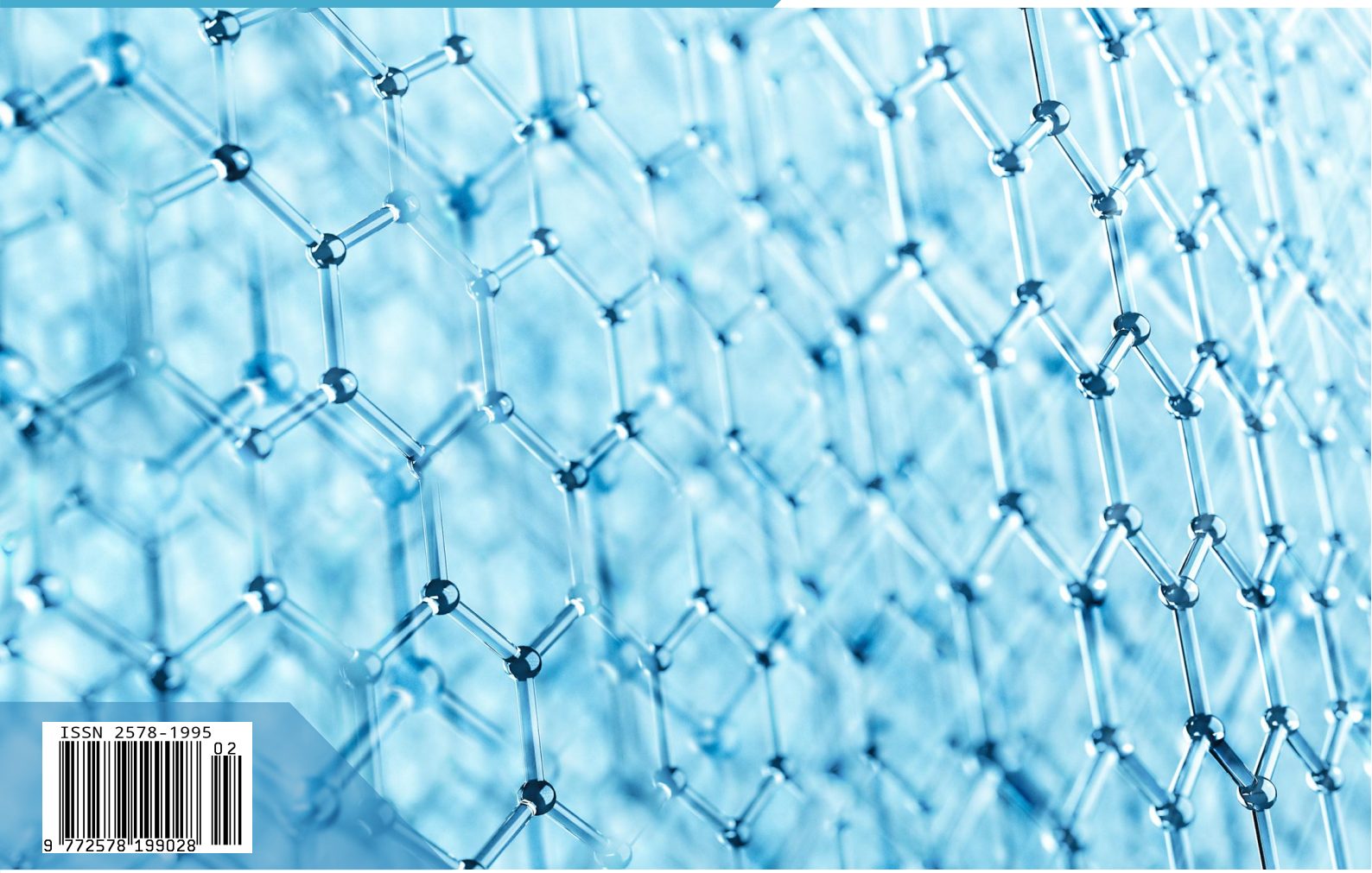

ISSN 2578-1995 02

9 772578 199028

EnPress Publisher

Editorial Board

Editor-in-Chief

Editorial Board Member

2019 | Volume 2 | Issue 2

Characterization and Application of Nanomaterials

https://systems.enpress-publisher.com/index.php/CAN/

Contents

Characterization and Application of Nanomaterials (2019) Volume 2 Issue 2
doi:10.24294/can.v2i2.627

ORIGINAL RESEARCH ARTICLE

The variations of hydrophilic self-cleaning properties and refractive index dependence in the ZrO_2 thin films by Gamma Irradiation

D. Abayli, N. Baydogan*

Energy Institute, Istanbul Technical University, Ayazaga Campus 34469, Istanbul, TURKEY. E-mail: dogannil@itu.edu.tr

ABSTRACT

ZrO_2 thin film samples were produced by the sol-gel dip coating method. Four different absorbed dose levels (such as ~ 0.4, 0.7, 1.2 and 2.7 Gray-Gy) were applied to ZrO_2 thin films. Hence, the absorbed dose of ZrO_2 thin film was examined as physical dose quantity representing the mean energy imparted to the thin film per unit mass by gamma radiation. Modification of the grain size was performed sensitively by the application of the absorbed dose to the ZrO_2 thin film. Therefore the grain size reached from ~50 nm to 87 nm at the irradiated ZrO_2 thin film. The relationship of the grain size, the contact angle, and the refractive index of the irradiated ZrO_2 thin film was investigated as being an important technical concern. The irradiation process was performed in a hot cell by using a certified solid gamma ray source with 0.018021 Ci as an alternative technique to minimize the utilization of extra toxicological chemical solution. Antireflection and hydrophilic properties of the irradiated ZrO_2 thin film were slightly improved by the modification of the grain size. The details on the optical and structural properties of the ZrO_2 thin film were examined to obtain the optimum high refractive index, self-cleaning and anti-reflective properties.

Keywords: Absorbed Dose; Irradiation; Optical Properties; Thin Film; Zirconium Oxide

ARTICLE INFO

Article history:
Received 27 June 2019
Received in revised form 23 July 2019
Accepted 25 July 2019
Available online 7 August 2019

1. Introduction

Thin films of zirconium oxide (ZrO_2) have attracted attention due to their advantageous properties for future thin layers technology. Zirconium oxide (ZrO_2) possesses good dielectric, optical, mechanical and chemical properties. Additionally, it exhibits high refraction index, very good transparency, great chemical stability and direct wide gap, with an optical band gap in the range of .0–5.85 eV[1,2]. Hence, ZrO_2 can be used in a wide range of applications such as optical filters, laser mirrors, barrier layers, buffer layers for super-conducting ceramics, as a biomaterial for prostheses, gas sensor, optical storage elements, scintillators and luminescent oxygen-sensors etc.[1,3]. Pure or doped ZrO_2 thin film continues to present sufficiently high thermoluminescence (TL) yield after irradiation with ionizing or ultraviolet (UV) radiation[3].

ZrO_2 thin films with different morphologies are prepared by several methods such as chemical vapor deposition (CVD), spray pyrolysis, reactive RF sputtering, polyol route, hydrothermal method bio-template method, ultra-sound assisted precipitation method, room temperature precipitation method, solution combustion method and sol–gel method[4,5]. Among these techniques, the sol–gel method can be used in the production of the thin films for electronics and optics. The sol-gel

method is of particular intere the production of the thin films for electronics and optics. The sol-gel method is of particular interest because of several advantages such as its simplicity, low processing temperature, stoichiometry control and its ability to produce uniform, chemically homogenous films and the formation of multi and mixed layers[1,2]. The sol–gel process involves the preparation of a "sol" (mostly colloidal), the transformation of the sol into a solid "gel" phase and crystallization by heating at increased temperatures (calcination). The first and second stages determine a chemical composition and the calcination stage controls the phase evolution of ZrO_2 from amorphous to nanocrystalline and crystalline phase transformation (monoclinic to tetragonal, etc.)[3]. The sol–gel process also allows the deposition of films and coatings with variable thickness from nm to micrometer, in an easy and fast way, by the use of either dip-, spin- or spray-coating procedures[6]. The ZrO_2 thin film can be produced with refractive indices *n* ranging from 1.35 to 2.50 and film thicknesses *d* from 150 to 1500 nm. The ZrO_2 thin film is hard, durable, and laser-damage-resistant thin films with high refractive index and it is widely used to produce multilayered coatings, also for the UV spectral range[7]

Generation of energy by using clean and environmental-friendly technologies is one of the major aims in industrial and scientific areas. Among the various coating techniques, the coating performed with sol–gel method is one of today's environment-protective methods. The sol-gel coating of ZrO_2 attracts attention since it is an environmental-friendly coating method[8]. As the $ZrOCl_2 \cdot 8H_2O$ is low toxicity of zirconium salts low toxicity of $ZrOCl_2 \cdot 8H_2O$ makes the use of $ZrOCl_2 \cdot 8H_2O$ attractive at the production of solution in this study. Hence it was possible to avoid the use of high level chemical toxicity by minimizing the production of hazardous chemical solution waste. Besides, more economical and environmentally friendly technologies are researched to adopt more eco-friendly thin film production methods in industrial and scientific areas. The utilization of irradiation treatment at several production steps can be preferred as a practical and rapid process to obtain the efficient performance in the devices containing thin film[9]. In this study, the ionizing radiation effect on structural and optical properties was used in the ZrO_2 thin film. Therefore, the improvements in the structural and optical properties were obtained, avoiding the production of extra hazardous chemical solution waste. The irradiation treatment by using the gamma radiation was a key parameter to manage the optical constants and the grain sizes of the ZrO_2 thin film to use them as protective and biomimetic layers. The agglomeration tendency of the irradiated grains at 0.7 Gy has resulted with high refractive index and more hydrophilic properties. There was a relation between the refractive index and hydrophilic properties with the rise of the grain size of the irradiated ZrO_2 thin film.

2. Experimental part

The sol-gel dip coating method at the production of the ZrO_2 thin film seems a candidate as more ecolabel coating method than other ZrO_2 thin film coating methods in the advance future economic coating technology for the industry[8].

$ZrOCl_2 \cdot 8H_2O$ is an attractive material in several procedures due to its low toxicity[10]. $ZrOCl_2 \cdot 8H_2O$ can be used for the environmentally friendly methods[11].

Hence, zirconium oxychloride octahydrate ($ZrOCl_2 \cdot 8H_2O$) inorganic precursor solution (Sigma Aldrich puriss grade, ≥99.0%) was used for the production of ZrO_2 thin films. All the substrates were cleaned with ethyl alcohol and rinsed with deionized water and they were sterilized with water vapour in an auto clave furnace (Nuve OT 012 Bench Top Steam Sterilizer) then dried at 100°C in drying oven (Binder ED 53). The solvent was determined as a mixture of 2-butanol and ethanol (in the ratio 1:1). Homogeneous solution including zirconium oxychloride octahydrate (2 wt.%) was produced by mixing 1 mol of zirconium oxychloride octahydrate in 1/3 of the total volume of mixed 2-butanol and ethanol. The solution was stirred for 45 minutes by use of a magnetic stirrer (Heidolph MR 3001K). Water for hydrolysis and nitric acid for oxidation (water: HNO_3: acetylacetone = 20: 0.4: 3) were added to the salt–alcohol solution. The stirring was continued for another 90 minutes to obtain

clear and transparent solution. The precursor solution prepared at 60°C deposited on cleaned soda-lime silicate glass substrates. Dip coater (KSV dip coater LMX2) with computer controlled was used and the dip coating parameters were chosen as 10 cm/min lifting speed and 90° vertical lifting. The dip coated films were dried at room conditions and pre-fired at 150°C. This process of coating and drying was repeated for 9 times in a heater. ZrO_2 film samples were annealed at 500°C for 1 h in air similar with the literature[12]. After the coating process, the remaining solution was stored in a dark glass bottle to prevent the degeneration of solution and used within 60 days at the refrigerator.

A certified Co-60 radioisotope was used as a gamma ray source emitting the photons with two different energies (1.17 MeV and 1.33 MeV) to examine the rise of the absorbed dose effect on the optical properties. Hence, the provided gamma ray beam was assumed as a monochromatic beam at ~ 1.25 MeV. The used Co-60 radioisotope had an activity level of 0.018021 Ci and it was determined as an appropriate irradiation source to evaluate the changes in the structural and optical properties of the ZrO_2 film samples. The absorbed dose level of the ZrO_2 thin film was the important parameter as the cumulative dose for the thin film samples at the irradiation area. The properties of the used Co-60 radioisotope were presented at the irradiation process of ZrO_2 thin film samples in **Table 1**.

Table 1. The properties of the Co-60 radioisotope used in the irradiation of ZrO_2 thin film

Radioisotope	K_γ (R m^2/Ci h)	A (Ci)	$T_{1/2}$ (y)	E_γ (MeV)
Co-60	1.32	0.018021	5.27	1.17 and 1.33

In this study, the ZrO_2 thin film samples were placed around the gamma irradiation source panoramically (in **Figure 1**). The cumulative dose level of the sample was considered as the total dose resulting from the repeated exposures of the ionising radiation. Because radiation fields can varies with several irradiation conditions (geometry or time) for a period of time[9]. Hence, four different absorbed dose levels were obtained such as ~ 0.4, 0.7, 1.2 and 2.7 Gy to examine the details of the changes in the optical and structural properties. All of the irradiation tests were conducted at room temperature.

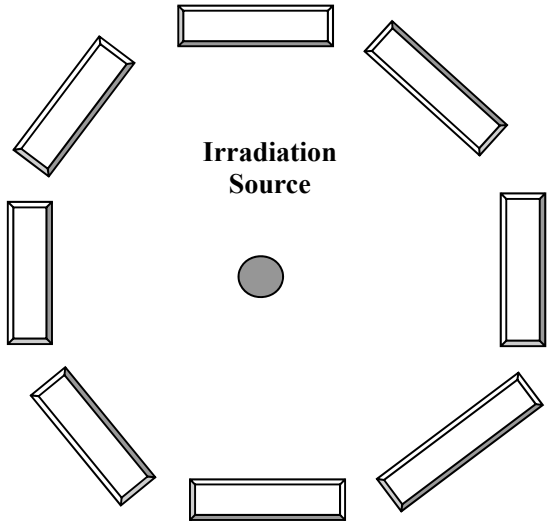

Figure 1. Irradiation settlement of the ZrO_2 thin film samples.

The thicknesses of the ZrO_2 thin film samples were determined by using Veeco Dektak 6M Stylus surface profilometer after the optical properties of ZrO_2 thin films prepared by sol-gel method were determined employing transmittance and reflectance spectrophotometry in UV and VIS range between 190–1100 nm by using PG Instruments T80 UV-VIS spectrophotometer. Thickness measurement was obtained from the coated to the uncoated part of the glass. Therefore, the thickness of the thin film was determined as ~ 80 nm[13]. The use of the ionizing radiation was a key parameter to limit the chemical solution toxicity without the generation of the extra hazardous chemical solutions at the environment.

3. Results and discussion

The surface morphology of the film was examined using 2D Scanning Electron Microscope (SEM). There were voids between the grains in some areas of surface as depicted in **Figure 2(a)-(d)**. The surface of the irradiated ZrO_2 thin film at 0.4 Gy was composed of the equaxial grains (~50 nm) in **Figure 2(a)**. The dimension of grains in which induced by gamma irradiation at 0.7 Gy had ~ 87.3 nm in **Figure 2(b)** and their dimension was the highest one with respect to the dimension of grains in other ones. The dimension of the grains was ~ 74.5 nm and decrease on the surface of the film at

1.2 Gy in **Figure 2(c)** and the dimension of grains is ~ 64.8 nm of the film at 2.7 Gy in **Figure 2(d)**. While the grains separated to more small grains due to the absorbed dose of the film, they started to gather and piled up at several places on the surface of the films at 1.2 Gy and 2.7 Gy. The changes of beta transmission of the ZrO_2 thin films supported the variation of the grain size in our previous study[13].

The properties of the surface started to change obviously at 0.7 Gy. The absorbed dose of 0.7 Gy was important to investigate the optical constants of the thin film. It was interesting to note that when the absorbed dose of the specimen reached to 1.2 Gy, the dimension of the grains decreased again. Moreover, the gathering of the grains in the induced film took place more obviously at the certain places. on the surface of the films in **Figure 2(c-d)**. The gathering of the grains at the surface of the film increased when the absorbed dose increased. But it was determined that there was the combination of grains with each other on the surfaces of irradiated specimens. The change of the valance state of impurity atoms in the irradiated thin film can be explained with the formation of new electronic order in defect centers as the result of the new configuration of the ions while the gathering of small grains with the rise of the absorbed dose in the thin film structure.

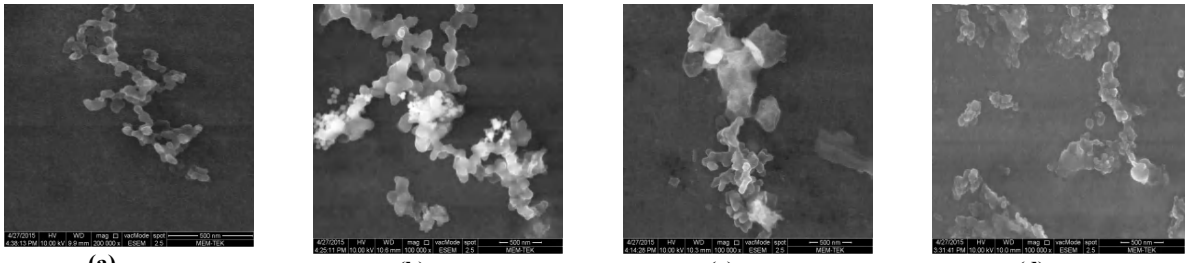

(a) **(b)** **(c)** **(d)**

Figure 2. SEM images of the ZrO_2 thin film irradiated at **(a)** 0.4 **(b)** 0.7 **(c)** 1.2 2.7 Gy**.**

The changes in transmittance (in **Figure 3**) and reflectance (**Figure 4**) of the irradiated ZrO_2 thin film samples were examined with the rise of the absorbed dose. The colour of the irradiated ZrO_2 thin film samples changed to darker colour tones with rise of the absorbed dose. The transmittance of the irradiated ZrO_2 thin films decreased with the rise of the grain size. Besides, the transmittance shifted towards the higher wavelength (red shift) in UV range as the absorbed dose increased. This behaviour is compatible with the decrease in transparency of the irradiated ZrO_2 thin films depending on the improvement of the optical absorbance. The red shift of the irradiated ZrO_2 thin film at 0.7 Gy (in **Figure 3**) distinguished clearly with the improvement of the optical absorbance (in **Figure 5**) as the irradiated thin film (at 0.7 Gy) reached maximum grain size from ~50 nm to 87 nm. However, there is not considerable information on the details of the changes in optical constants of the irradiated ZrO_2 thin film by gamma radiation in previous studies[14]. The rise of the grain size resulted with the decrease of the optical transmittance of the irradiated thin film (at 0.7 Gy). The rise of the grain size resulted with the decrease of the reflectance of the ZrO_2 thin film. The minimum reflectance of the thin film irradiated at 0.7 Gy was determined at the film with maximum grain size reached from ~ 50 nm to ~ 87 nm. The reason of this was the decrease of the grain boundaries around the course grains. The changes in refractive index of the ZrO_2 thin film samples irradiated at different absorbed dose levels were determined from the transmittance according to Swanepoel's envelope method in this study. The details on the determination of the refractive index were presented in the previous studies[15]. The interference fringes shifted towards the higher wavelength (red shift) region. Swanepoel's envelope method stated the minimum and maximum envelops of transmittance spectrum in the weak and medium absorption regions; extrapolating the graph of the refractive index at the strong absorption region in the literature[16]. The optical constants of ZrO_2 thin films were affected by the gamma irradiation. It was possible to determine the changes in optical constants such as the refractive in-

dex (n) (in **Figure 6**), extinction coefficient (k) (in **Figure 7**) and absorption coefficient (α) (in **Figure 8**) with the rise of the grain size in this study. There were the increases in n, k and α values of the irradiated ZrO_2 thin film as the result of the increase in grain size (in **Figure 2**). The rises of n, k and α were related with the enhancement of optical absorption as the result of the controlling of the absorbed dose. The increase of the optical constants of the irradiated films was related with the gathering of the grains at the surface of the film with the controlling of the absorbed dose according to the SEM images (in **Figure 2**). Photoluminescence (PL) studies provide information about the electronic band transitions, structure, defects and chemical composition of the optical materials[2]. The exciton lumenescence and intrinsic defects related luminescence are known in a number of oxides. For ZrO_2, the photoluminescence is of much interest for both theoretical and experimental investigations. There are some references to make an evaluation between the results of this study and results in literature by using different irradiation sources. A broad PL emission is observed at ~ 480 nm for ZrO_2 structures after the samples are induced by UV irradiation in the literature[2]. The refractive index increases with the reduction of the transmittance of the films as the absorption region of the transmitance spectra rises towards higher wavelenght region, in the previous study of Berlin *et al*.[5]. In this study, it was determined that there were the dramatic changes in optical constants at ~ 480 nm. The photoluminescence effect at ~ 480 nm supported the rise of the optical transmittance and decrease of the optical absorbance slightly depending on the increase of the scattered photons. Besides, the decrease of the optical absorbance has led the decrease of the optical constants over ~ 480 nm. It was thought that the improvement of the grain sizes in irradiated ZrO_2 thin film at 0.7 Gy indicated the enhancement of the photoluminescence effect dominantly at the coarse grains with 87 nm.

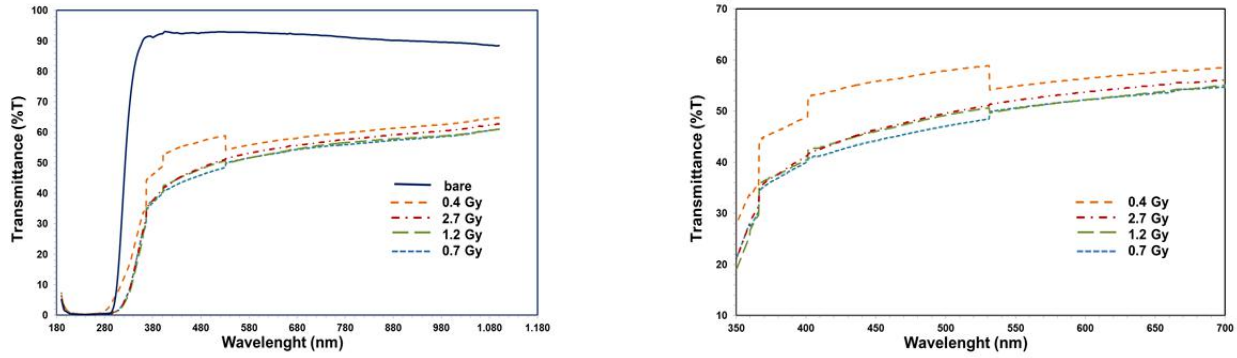

Figure 3. (a) The changes in transmittance of the irradiated ZrO_2 thin film; **(b)** the details on the changes in the transmittance.

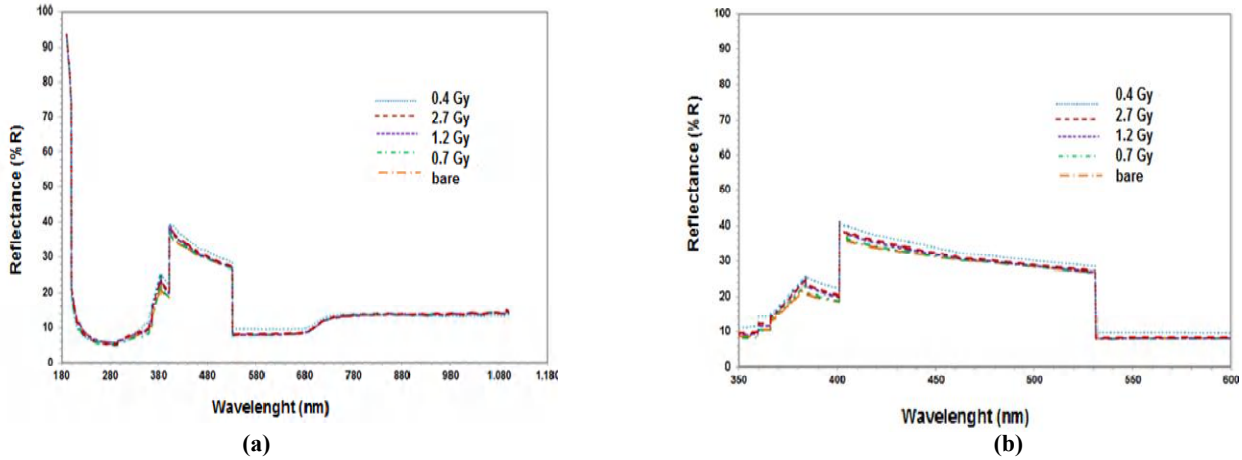

Figure 4. (a) The changes in reflectance of the irradiated ZrO_2 thin film; **(b)** the details on the changes in the reflectance.

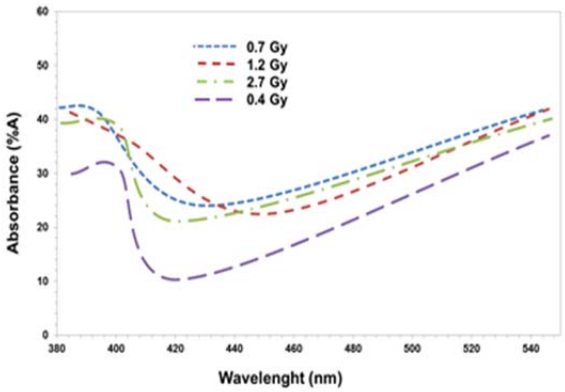

Figure 5. The changes in optical absorbance of the ZrO_2 thin film.

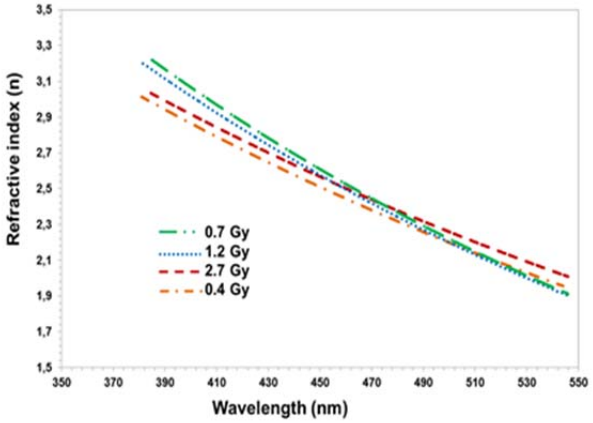

Figure 6. The changes in the refractive index, n of the irradiated ZrO_2 thin films.

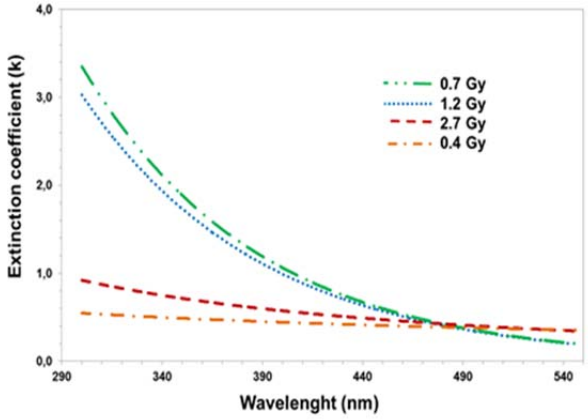

Figure 7. The changes in extinction coefficient, k of the irradiated ZrO_2 thin film.

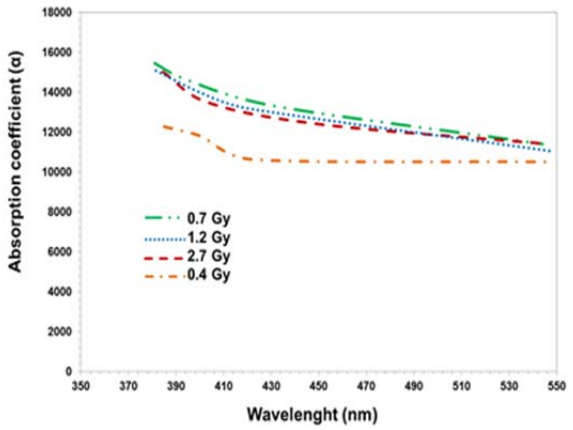

Figure 8. The changes in absorption coefficient, of the irradiated ZrO_2 thin film.

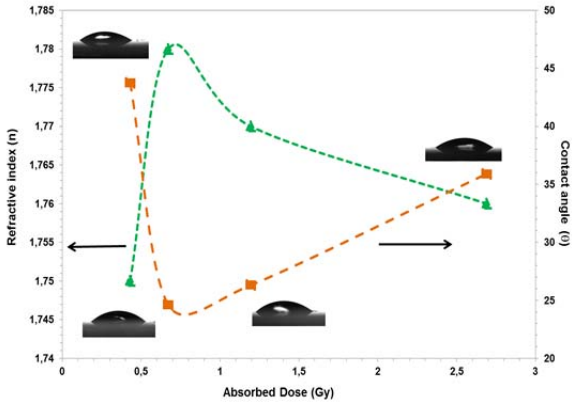

Figure 9. The relation between static water contact angle and refraction index of the ZrO_2 films.

The surface contact angle of the ZrO_2 thin film was determined by using a contact angle measurement instrument. The contact angle values of the thin film decreased slightly and a minimum value of around 24.62° was obtained with the increase of the grain size when the absorbed dose was set to 0.7 Gy. The rise of the grain size led to increase the surface roughness and the decrease of contact angle values of the thin film resulted with the improvement of the hydrophilic properties. Hence, the contact angle was decreased by irradiation and wettability of hydrophilic nanostructured ZrO_2 surface was modified slightly with increasing surface roughness. The nanoscale roughness having coarse grains (~87 nm) has influenced the surface wettability slightly at 0.7 Gy. The ZrO_2 thin film derived on soda-lime glasses has presented a relation between the refractive index and hydrophilic properties as the result of the change in the size of the grains.

4. Conclusions

The ZrO_2 thin film was derived from $ZrOCl_2 \cdot 8H_2O$ (which is low toxicity of zirconium salts) by using sol-gel dip coating method as it is a green friendly alternative coating method. The irradiation treatment has played a role in the enhancement of the optical constants (such as refractive index, the extinction coefficient and absorption coefficient) of the ZrO_2 thin film. The improvement in the irradiated grain size supported to rise the refractive index by minimizing the production of hazardous chemical solutions. The rise of the grain size of the irradiated ZrO_2 thin film improved the optical constants. There was a relation between the induced optical constants and the gathering of the irradiated grains by gamma radiation. The red shift in UV range by using gamma irradiation was enhanced with the rise of the grain size. It was possible to control the dimension of grains with the applied absorbed dose. The agglomeration tendency of the irradiated grains has enhanced slightly the refractive index and hydrophilic properties of the ZrO_2 thin film. The grain size reached a maximum value from ~50 nm to 87 nm when the absorbed dose of ZrO_2 thin film attained to 0.7 Gy.

References

1. Bensouyad H, Sedrati H, Dehdouh H, *et al*. Structural, thermal and optical characterization of TiO_2: ZrO_2 thin films prepared by sol–gel method. Thin Solid Films 2010; 519(1): 96–100.
2. Joy K, Berlin IJ, Nair PB, *et al*. Effects of annealing temperature on the structural and photoluminescence properties of nanocrystalline ZrO_2 thin films prepared by sol–gel route. Journal of Physics and Chemistry of Solids 2011; 72(6): 673–677.
3. Chernov V, Belykh A, Meléndrez R, *et al*. Beta radiation induced thermoluminescence in pure ZrO_2 prepared by sol–gel. Journal of Non-Crystalline Solids 2006; 352(23-25): 2543–2547.
4. Ravichandran AT, Catherine S, Ravichandran K, *et al*. Effect of Al doping on the structural and optical properties of ZrO_2 nanopowders synthesized using solution combustion method. Superlattices & Microstructures 2014; 75: 533–542.
5. Berlin IJ, Lekshmy SS, Ganesan V, *et al*. Effect of Mn doping on the structural and optical properties of ZrO_2 thin films prepared by sol–gel method. Thin Solid Films 2014; 550: 199–205.
6. Garcia RBR, Silva FS, Kawachi EY. New sol–gel route for SiO_2/ZrO_2 film preparation. Colloids and Surfaces A: Physicochemical Engineering Aspects 2013; 436: 484–488.
7. Jerman M, Qiao Z, and Mergel D. Refractive index of thin films of SiO_2, ZrO_2, and HfO_2 as a function of the films' mass density. Applied Optics 2005; 44(15): 3006–3012.
8. Li Q, Zhong X, Hu J, *et al*. Preparation and corrosion resistance studies of zirconia coating on fluorinated AZ91D magnesium alloy. Progress in Organic Coatings 2008; 63(2): 222–227.
9. Baydogan N, Ozdemir O, Cimenoglu H. The improvement in the electrical properties of nanospherical ZnO: Al thin film exposed to irradiation using a Co-60 radioisotope. Radiation Physics & Chemistry 2013; 89: 20–27.
10. Mishra S, Ghosh R. Ecofriendly and sustainable efficient synthesis of bis(indolyl)methanes based on recyclable Brønsted (CSA) or Lewis ($ZrOCl_2.8H_2O$) acid catalysts. Indian Journal of Chemistry; 2011; 50: 1630–1636.
11. Jafarpour M, Rezaeifard A, Heidari M. A new catalytic method for eco-friendly synthesis of quinoxalines by zirconium (IV) oxide chloride octahydrate under mild conditions. Letters in Organic Chemistry 2016; 8(3): 202–209.
12. Berlin JI, Lakshmi JS, Lekshmy SS, *et al*. Effect of sol temperature on the structure, morphology, optical and photoluminescence properties of nanocrystalline zirconia thin films. Journal of Sol-Gel Science and Technology 2011; 58(3): 669–676.
13. Abayli D, Baydogan N. The characterization of the irradiated ZrO_2 transparent thin films. Procedia — Social and Behavioral Sciences 2015; 195: 2117–2121.
14. Abayli D, Baydogan N. The changes in optical absorbance of ZrO_2 thin film with the rise of the absorbed dose. Book of Abstracts of 9th International Physics Conference of the Balkan Physical Union. Istanbul, TR; 2015 August 24-27. p.175.
15. Baydogan N, Ozdurmusoglu T, Cimenoglu H, *et al*. Refractive index and extinction coefficient of ZnO: Al thin films derived by sol-gel dip coating technique. Defect and Diffusion Forum 2013; 334-335: 290–293.
16. Larijani MM, Hasani E, Safa S. Annealing temperature effect on the optical properties of thermally oxidized nano-crystalline ZrO_2 thin films grown on glass substrates. Applied Surface Science 2013; 290: 490–494.

Characterization and Application of Nanomaterials (2019) Volume 2 Issue 2
doi:10.24294/can.v2i2.644

ORIGINAL RESEARCH ARTICLE

Synthesis and characterization of electrically conductive silicone rubber — TiB_2 composites

Aparna M Joshi[1*], Anjali A Athawale[2]

[1]*K.D. Joshi Rubber Industries Pvt. Ltd. -A-82-85, H Block, MIDC, Pimpri, Pune 411018, India. E-mail: aparnamjoshi @rediffmail.com*

[2]*Department of Chemistry, University of Pune, Pune 411 007, India.*

ABSTRACT

In this paper, electrically conductive composites comprised of silicone rubber and titanium diboride (TiB_2) were synthesized by conventional mixing methods. Fine particles of TiB_2 (in micron size) and 10 parts per hundred parts of rubber (phr) proportion of carbon black (XC-72) were used to make the composites with HTV silicone rubber. The composites were cured at appropriate temperature and pressure and the effect on the electrical properties was studied. The resistance of the silicone rubber is ~ $10^{15}\Omega$ which decreases to 1–2 kΩ in case of composites with negligible effect of heat ageing. The hardness increases by ~ 35% simultaneous to the decrease of ~ 47% in the tensile strength. Morphological characterization indicates the homogeneous dispersion of the fillers in the composite.

Keywords: Silicone Rubber; Electrical Conductivity; Titanium Diboride; Composite

ARTICLE INFO

Article history:
Received 18 July 2019
Received in revised form 12 August 2019
Accepted 16 August 2019
Available online 3 September 2019

1. Introduction

Electrically conductive silicone rubber composites have great potential towards various applications[1], such as rollers used in printing, fibre weaving, conductive coatings, electronics communication industry, light emitting devices, gas and pressure sensors, EMI shielding etc. Silicone rubber, as an insulating material, has very large application horizon and inducing electrical conductivity into such a versatile material is adding to its value. Electrically conductive composites of silicone rubber with conductive carbon such as XC-72 are well known and can be easily synthesized using conventional mixing methods. XC-72 imparts electrical conductivity to the composites by tunnelling effect of the free electrons on carbon from one aggregate to another through the polymer molecules[2]. These electrons interact with polymer and also with the peroxide used as the curing agent when the composites are subjected to temperature or prolonged storing. Other conductive materials that are reported to impart electrical conductivity to the rubbers are metal powders and graphite etc. The limitations to the use of metal powders are poor process ability of the composites[3,4]. Graphite, when used in rubbers, renders conductivity to the composites, however upon high temperature curing of the composites, the conductivity is lost due to penetration of polymer molecules into graphite layers[5,6]. TiB_2-silicone rubber composite is reported as a piezoresistive material with 70 % of TiB_2[7]. Similar to the metal powders, the ease in the process ability of the composites is reduced. TiB_2 is stable chemi-

cally, thermally and physically with a superconductive behaviour at cryogenic temperatures[8].

In the present work, an electrically conductive ceramic material, TiB_2, has been used in conjugation with XC-72 to synthesize conductive composites (SITB). The resultant composites are thermally stable with very good physical and electrical properties under ambient conditions.

2. Experimental

Silicone rubber grade TSE 221-3-U from Momentive Performance Ltd., Japan, TiB_2 with mean particle size of 14 µm from Momentive India, XC-72 from Cabot corporation-India and Luperox 101-45 were used for synthesizing the composites. The composites were prepared on a two roll laboratory mixing mill. The silicone rubber was first masticated for few minutes followed by addition of 10 phr of XC-72, 5 phr of TiB_2 and 1.8 phr of Luperox–101/45 slowly one after the other with continuous rolling on mill. After complete addition, the whole mass was rolled again for 5-10 minutes to attain homogeneity and form a nice band on the mill. The composites were cured by compression moulding in appropriate moulds at 170ºC for 10 mins, and characterized for their electrical, mechanical, morphological and thermal properties after cooling the specimens to room temperature. The specimens were kept as such for 24 hrs before the testing was carried out.

3. Characterization

3.1 Electrical conductivity

Surface resistance was measured by using a 2 probe digital Multimeter from Agilent with 1 cm distance between the probes. Surface resistance of samples was measured both before and after curing. In rubber elastomers, the surface resistance was measured as the surface may conduct electricity more easily than the bulk[9,10].

3.2 Electrical conductivity after heat ageing

The influence of heat ageing on the conductivity of the samples was investigated at 90ºC for 100 hrs in oven. The resistance of the samples was recorded at an interval of 3 hrs.

3.3 Specific gravity

ASTM standard D297–93–Hydrostatic weighing method was utilized for specific gravity measurements with a ratio of mass of a unit volume of composite to mass of a unit volume of water.

3.4 Hardness

The specimens with 6 mm diameter and thickness both were loaded on Type–2 durometer Shore A operating stand to measure the hardness in Shore A by ASTM standard D 2240 method. GSE Testing Instrument with indenter of type “A” was used for measuring the hardness.

3.5 Tensile strength

Computerized Tensile Testing machine by Star Testing Systems was used for measuring the tensile strength by ASTM standard D-412 method. A sheet of size 150×150×2 mm^3 was used to prepare five dumbbell shaped specimens which were punched in a Die–C. Punching machine was used to get a single impact stroke, the strength of all five specimens were measured, the extreme high and extreme low readings were discarded and average of three specimens were taken.

3.6 Tear strength

ASTM standard D-624 was adopted for tear strength testing. Three dumbbells were punched from the sheet of same size as that for tensile strength with a single impact stroke punching machine to ensure smooth cut surfaces in Die-C with dimensions as per ASTM standard D-624. These specimens were tested and average of them was taken. Tear strength was measured on Star Testing Systems-Mumbai machine.

3.7 Rebound resilience

Rebound resilience was tested using ASTM standard D 2632-01. The specimen of 12 mm thickness and 6 mm diameter was used. Impact resilience was measured by Vertical Rebound Resiliometer by The Shore Instrument and Manufacturing Co., Mumbai, India.

3.8 Morphological characterization

Very thin films of 0.5×0.5 cm were cut from the cured samples and coated with platinum for

scanning under JEOL-JSM 6360A electron microscope from Japan for SEM analysis.

3.9 Swelling resistance

The degree of swelling in solvents is the key property in case of polymer composites. The solvent used for testing the swelling resistance was ASTM Fuel B, which is a combination of 70% isopropyl alcohol and 30% toluene. Specimens of 1.5cm×2cm×2mm were weighed and immersed in the solvent for 24 hrs. The difference in the weight of specimens in air and water before and after immersion were recorded. The solvent resistance was measured using the equation (1):

$$Q = \frac{W_i - W_0}{W_0} \times 100 \qquad (1)$$

Where Q represents the degree of swelling; W_i and W_0 represent the mass of specimen before and after immersion in the solvent respectively.

3.10 Thermal characterization (TGA)

Thermograms of the specimens were recorded on the thermogravimetric analyser model TA-60 WS of Shimadzu—Japan in the range between RT-1000°C at a scanning rate of 10°C min^{-1} under nitrogen atmosphere with a flow rate of 50 ml min^{-1}.

4. Results and discussion

The electrical resistance of virgin silicone rubber is known to be ~$10^{15}\Omega$. When TiB_2 along with XC-72 is added to this material, the resistance was observed to decrease by an order of ~$10^{12\text{-}13}\Omega$. Various proportions of XC-72 and TiB_2 were added to silicone rubber, however, in order to achieve conductive composites optimum proportion of XC-72 and TiB_2 was found to be 10 phr and 5 phr respectively. The surface resistance of the composite was recorded to be 15-18 kΩ.

TiB_2, being a ceramic material, has good thermal stability. SITB composites are observed to show a negligible loss in the electrical conductivity when subjected to 90°C for 100 hrs, as is shown in **Figure 1**. There is a loss of ~2-3 kΩ in the resistance of the specimens of SITB at these conditions of temperature and time. **Figure 1** depicts the changes in the surface resistance upon heat ageing.

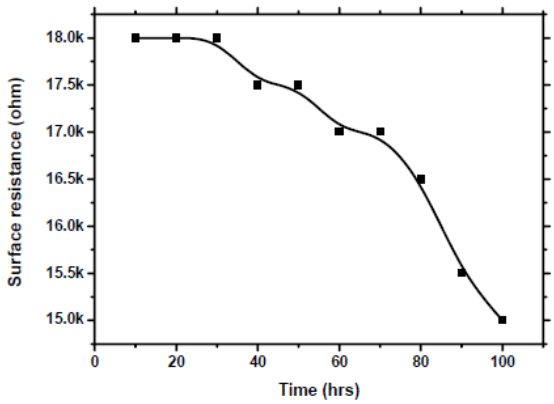

Figure 1. Effect of heat ageing on surface resistance of SITB composite.

The specific gravity of the composites is increased to some extent. Addition of TiB_2 and XC-72 enhances the specific gravity. Blank silicone rubber has a specific gravity of 1.07 while that of the composite is 1.14.

The ceramic material — TiB_2 is extremely hard (as hard as diamonds). This property is seen to be reflected in the hardness of the composites. The hardness of silicone rubber is 40 Shore A. Hardness of silicone rubber with carbon alone is 45 Shore A and that along with TiB_2 is 50 Shore A.

Every component in a composite contributes to the tensile strength of the composite and is the maximum stress experienced by the composites when stretched at the point of rupture. Tensile strength is the property of elastic materials; and addition of non-elastic fillers reduces this property. TiB_2, as a hard-ceramic material, resists stretching and ultimately reduces the tensile strength of the composite. The composites show ~ 47% reduction in tensile strength compared to silicone rubber with a standard deviation in the value of ± 1.1.

Tear is initiated in rubbers at the notch in the specimen and depends on the filler-matrix interaction. Stronger interaction leads to a higher tear strength. In the case of SITB composite, the tear strength is observed to increase compared to the blank silicone rubber. This can be attributed to the better interaction between TiB_2 and the silicone rubber. The tear strength of the composite is 15 kNm^{-1} with the standard deviation of ± 0.50.

The rebound resilience shows an inverse proportion to hardness of rubber material. In case of SITB composites, the rebound resilience is decreased to 39 % from 67% for the blank rubber. Hard-

ness of TiB_2 affects the elasticity of the composite, thereby decreasing the rebound impact.

Homogeneity of the composites can be observed from the scanning electron microscopic image shown in **Figure 2**. A homogeneous dispersion of TiB_2 in the rubber matrix leads to the better interaction between the materials leading to the rise in electrical conductivity which is the result of inter particle connection and also increases the physical properties such as hardness and tear strength.

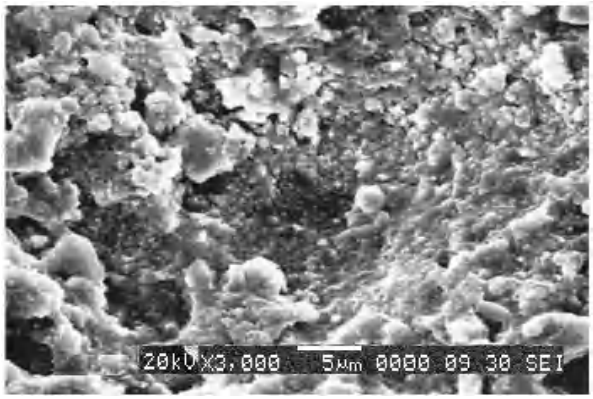

Figure 2. SEM image of the composite SITB**.**

Degree of swelling is the indication of the crosslinking density of the polymer composites. The lower the swelling is, the higher the crosslinking density will be. In case of SITB composites, lower degree of swelling shows the compactness and good filler-matrix interaction. Lower degree of swelling of the composites in ASTM Fuel B extends the application potential for high efficiency electronic devices[11]. The degree of swelling is decreased in case of composites than the silicone rubber itself. This can be attributed to the homogeneous dispersion which leads to the better filler-matrix interaction. The solvent resistance of the composite is 11% and that of blank silicone rubber is 17%. **Figure 3** depicts the scanned electron microscopic image of the composite after immersion in ASTM Fuel B for 24 hrs. The voids are due to the solvent penetration into the matrix. Thermal properties of the composites are negligibly altered as the proportion of TiB_2 added is very small.

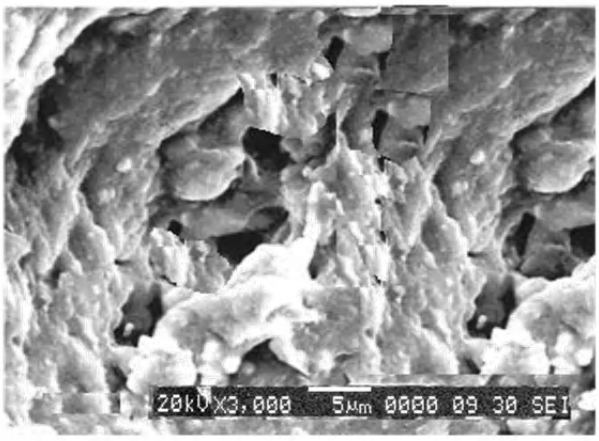

Figure 3. SEM image of the composites after swelling**.**

As can be seen from **Figure 4**, when the temperature is up to 450ºC, there is a weight loss due to volatile matter and decomposition of organic matter. When the temperature is between 450ºC and 600ºC, the sharp change in weight is due to the decomposition of silicone rubber into silicon and oxygen. The weight gain of ~ 4 % above 600ºC as is seen in **Figure 3** can be attributed to the oxidation of TiB_2 to form TiO_2[12]. TiB_2 combines with the oxygen generated during the decomposition of silicone rubber polymer.

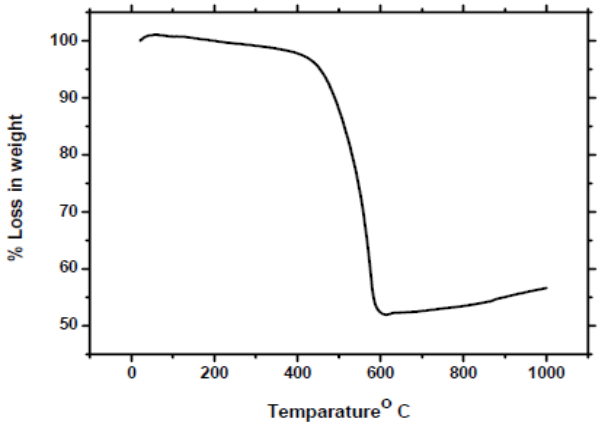

Figure 4. Thermogram of SITB composite**.**

5. Conclusions

Incorporation of TiB_2 and XC-72 into the silicone rubber gives an electrically conductive composite with the surface resistance of 15–18 kΩ under ambient conditions with a negligible effect of heat ageing on the surface resistance. The hardness and tear strength of the composites are increased with a decrease in the tensile strength and rebound resilience. The composites show an excellent resistance to the solvent — ASTM Fuel B.

Acknowledgements

The authors are thankful to K.D. Joshi Rubber Industries Pvt Ltd. for supporting the project. And the authors would like to extend sincere gratitude to University of Pune — Department of Chemistry for providing the facilities and Department of Physics for SEM facility.

References

1. Kathirgamanathan P. Light-coloured conductive fillers for the production of charge dissipative polymers. Polymer 1993; 34(7): 1549–1550.
2. Norman RH. Conductive rubbers and plastic. London: Elsevier publishing Co. Ltd.; 1970. p. 169–170.
3. Bhattacharya SK (editor). Metal-filled polymers: Properties and applications. New York: Marcel Dekker, Inc.; 1986. p. 355.
4. Gwaily SE, Nasr GM, Badawy MM. Thermal and electrical properties of irradiated styrene butadiene rubber-Metal composites. Egyptian Journal of Solids 2001; 24(2): 193–205.
5. Rajatendu S, Mithun B, Bandopadhyay S, *et al*. A review on the mechanical and electrical properties of graphite and modified graphite reinforced polymer composites. Progress in Polymer Science 2011; 36(5): 638–670.
6. Pan Y, Yu Z, Ou Y, *et al*. A new process of fabricating electrically conducting nylon 6/graphite nanocomposites via intercalation polymerization. Journal of Polymer Science B: Polymer Physics 2000; 38 (12): 1626–1633.
7. Jeong DY, Ryub J, Lima YS. *et al*. Piezoresistive TiB_2/silicone rubber composites for circuit breakers. Sensors and Actuators A: Physical 2009; 149(2): 246–250.
8. Tantawy FE. The interrelation among network structures, molecular transport of solvent, and creep behaviors of TiB_2 ceramic containing butyl rubber composites. Journal of Applied Polymer Science 2005; 98(5): 2226–2235.
9. Smith LP. The language of rubber: An introduction to the specification and testing of elastomers. 1st ed. London: Butterworth-Heinemann Ltd.; 1993. p. 257.
10. Blythe AR. Electrical resistivity measurements of polymer materials. Polymer Testing 1984; 4(2-4): 195–209.
11. Tantawy FE. Influence of solvent transport on physico-chemical properties of crosslinked butyl rubber filled with TiC ceramic. Polymer Degradation and Stability 2001; 73(2): 289–299.
12. Sood DK, Mukherjee S, Katselis G, *et al*. Modification of high-temperature oxidation of titanium diboride films by implantation with tantalum and titanium ions. Surface and Coatings Technology 1998; 103-104: 304–31.

Characterization and Application of Nanomaterials (2019) Volume 2 Issue 2
doi:10.24294/can.v2i2.835

ORIGINAL RESEARCH ARTICLE

From atomic-scale interfaces — To new nanomaterials

Nikolay Plusnin*

Institute of Automation and Control Processes, Far East Branch, Russian Academy of Sciences, Vladivostok 690041, Russia. E-mail: plusnin@dvo.ru

ABSTRACT

The problem of the synthesis of new type nanomaterials in the form of nano-coatings with sub-nanometric heterogeneity has been formulated. It has been presented an analysis of influences of physical vapor deposition in ultrahigh vacuum on the process of intermixing a film with a substrate, including the results, which has been obtained under the formation of transition metal – silicon interface. The generalization of the obtained experimental results develops an approach to the development of new nano-coatings with low-dimensional heterogeneity. The principles of constructing such low-dimensional nano-coatings, their properties and possible applications are considered.

Keywords: Low-dimensional Nano-coating; Structure; Forming; Properties; Application

ARTICLE INFO

Article history:
Received 13 November 2019
Received in revised form 7 December 2019
Accepted 9 December 2019
Available online 25 December 2019

1. Introduction

In the world, there are many large scientific educational and technical centers which are engaged in research and various applications of nanotechnology. In addition, there are a number of manufacturers of nanophase materials. The most famous among them is the company "Nanophase Technologies", which produces nano-dispersed powders based on zinc oxide "NanoGard" and aluminum oxide "Nano-Tech"[1].

Usually, nanophase materials that consist of nano-dispersed particles are produced from particles or atomic clusters with a diameter of 2 to 50 nm by packing them in bulk materials with a grain size of 4 to 30 nm. In terms of their atomic structure, these materials are neither amorphous nor crystalline, nor even quasi-crystalline. They are in some intermediate low-dimensional state, the so-called nanophase state. The technology for the production of nanophase materials, which use compacting nano-dispersed powders, is relevant to the present day.

Nevertheless, nanophase materials in the form of nano-coatings are needed to create promising systems of nano-industry in electronics, optoelectronics, telecommunication, healthcare, biotechnology, metallurgy, metalworking, power engineering, machine and instrument engineering, construction and industrial materials, chemistry and petrochemistry, as well as in analytical instrumentation, nano-electronics, nano-photovoltaics, nanomedicine and in a number of other devices.

These nano-coatings can have a set of unique properties that are absent in bulk or massive nano-coatings. In particular, they can be realized in the low-dimensional nano-metrical (LDNM) state of matter with characteristic sizes of inhomogeneities from atomic (0.1 nm) to 1nm, reducing the size of the inhomogeneities to such limits will lead

to a significant increase in the low-dimensional effects.

The low-dimensional nature of the electronic and atomic structure and properties of LDNM coatings will be supplied due to the heterogeneous or heterophase (with low-dimensional inclusions) structure of nano-coatings, the close-acting boundary effects, surface effects, and also due to the quantum-size effect (QSE).

The problem of creating LDNM coatings is associated with the methods of synthesis of these coatings and also with the methods of diagnostics of their structural-phase state and properties, both in the process of obtaining these nano-coatings and at its completion. Combining the synthesis and control of LDNM coatings in ultrahigh vacuum environment allows purposely and effectively search for new nano-coatings by reducing the cycles of controlling their structure and properties.

Ultrahigh vacuum (UHV) is the most convenient medium for controlling the atomic and electronic structure and various properties of coatings. UHV allows synthesizing coatings from atomic beams (molecular-beam growth)[2] and use focused electron, ion and photon beams for the diagnostics of coatings[3]. Therefore, combining the synthesis and control of coatings in a vacuum is very important. In addition, UHV vacuum provides the ability to control the surface state of coatings during their synthesis and makes it possible to do this cyclically to control the formation of hyperfine layers and their interfaces, creating the necessary composition and structure in them.

At present, methods and apparatus for the synthesis and control of coatings in vacuum have developed significantly and reached a high level of perfection[4]. This allows, basically, focusing not on the creation of these methods, but on their use.

Nevertheless, the specificity of LDNM coatings, their nonequilibrium, and sub-nanostructured state, requires more precise regulation of growth parameters and over a wider range of their values than modern methods allow. In particular, it is necessary to develop methods for producing directed atomic beams, which will possess not only a low but also a high density and, simultaneously, not only a high, but also a low temperature or kinetic energy.

In addition, the structural-phase specificity of LDNM coatings, which differ on their atomic density and atomic configuration from bulk phases, requires the further development of more adequate methods for monitoring their structural-phase state during the synthesis, including electron spectroscopy and diffraction.

Therefore, it is necessary to improve these methods and adapt them to growth control at the sub-nanometric spatial scale and real time. Solving all these problems will allow the creation of novel nano-coatings in the nanophase state in the form of low-dimensional monolayer or multilayer LDNM coatings.

2. Formation, structure, properties and applications of low-dimensional nano-coatings

2.1 Vacuum low-thermal vapor deposition

In the methods of thermal vapor-phase physical deposition in vacuum, a decrease in the thickness of films and a decrease in the width of their interface with a substrate (due to decrease of mixing with the substrate) is achieved in the vast majority of cases by a decrease in substrate temperature[5]. However, for LDNM coatings, this is not sufficient because the high vapor kinetic energy and latent heat of the film surface phase transition lead to mixing and compound formation at the interface[6].

New methods that have solved this problem are evaporation with a lowered vapor temperature during the growth of LDNM coatings from this vapor[6,7], as well as modification of the interaction of the film with the substrate by a monomolecular intermediate layer[8]. In addition, methods have been improved to control the growth of LDNM coatings[7,9,10].

2.2 The approach to the formation of low-dimensional nano-coatings in a vacuum

The specificity of this approach is connected with the mutual compatibility of two technologies: ultrahigh-vacuum technology (UHVT) and nanotechnology (NT). Both technologies relate to the advanced field of applied science and technology

and use controlled manipulation of individual particles, including atoms and molecules.

The main goal of this approach is to search for and synthesize new low-dimensional nano-coatings, using thermal vapor-phase physical deposition in an ultrahigh vacuum. Nano-coatings are expected to be used in nano-industrial areas where large amounts of coatings (more than 1 nm thick) do not need to be used. Namely, the coating consists of tightly packed nanoparticles in a disordered or ordered composite structure and can be made in the form of a non-equilibrium and metastable single-layered or multilayered film of nanometric thickness.

To accomplish this goal, it is necessary to modify the methods for obtaining atomic beams in vacuum and to further develop methods of electron spectroscopy, microscopy, and probe measurements.

In vacuum, or on the surface of a solid in vacuum, particle beams and fields can interact without interference. This property gives UHVT a unique advantage over NT in other environments. First of all, this is the controllability of the synthesis of LDNM coatings. Another important advantage of UHVT is the clean conditions for the synthesis of LDNM coatings.

As for the lower level of the practical application of UHVT because of the high cost, it is compensated by either the high cost of the product (for example, in nanomedicine) or the ability to produce the product in the form of films on large substrates, for example, in solar energy, microelectronics and nano-electronics.

The approach to low-temperature vaporphase synthesis of nano-coatings is as follows[11]:

1) Development of principle for designing the electronic and atomic structures of LDNM coatings based on the interface between the nano-coating and the substrate and the modification of the interface between the particles in the nano-coating.

2) Development of the principle of utilizing the hidden energy of LDNM coatings as an additional spontaneous heat source during solid phase reaction and crystallization of nano-coatings. .

3) Development of the principle of using LDNM coatings to connect constituent and heterostructured nanoparticles and substrates in solid phase vacuum sintering and welding.

4) Development of the principle for controlling growth of LDNM coatings from high density, low temperature beams.

5) Development of the principle for atomic and nano-controlled structural physical and electrophysical properties of LDNM coatings.

To implement this approach, it is necessary to conduct both theoretical studies, including computer modeling and experimental studies.

It is assumed that the main application of LDNM coatings will be concentrated on electronics and communications, as well as on nanoelectronics, nanospintronics, nanooptics, nanoplasmonics, and analytical instrumentation in ecology, biology and medicine.

In the near future, it is possible to predict the creation of new LDNM coatings with record conductivity, magnetization, coercitivity, reflection coefficient, and refraction index and excitation efficiency of surface plasmons. These materials will allow creating new instruments and environmentally friendly technologies for converting, processing, transferring and storing information and energy.

2.3 Low-dimensional nano-metric thickness coatings

As already mentioned, the low-dimensional nature of the electronic and atomic structure and properties of LDNM coatings is formed due to the heterogeneous or heterophase (with inclusions of low-dimensional particles) structure of nano-coatings, the boundary effects of close-acting of substrate and vacuum and QSE.

This approach to the structure of LDNM coatings allows us to highlight principles of organization of the LDNM coatings structure, namely, their types and character of influence on their properties:

1) Heterogeneous LDNM coatings with intercrystalline proximity effect.

2) Heterophasic LDNM coatings with interfacial proximity effect.

3) LDNM coatings with effects of interfaces with substrate and vacuum.

4) LDNM coatings with quantum size effect due to cross-border interaction.

5) LDNM coatings with quantum size effect, which has caused by the limitation of the internal

space of particles.

Depending on the combination of these five principles of organization, different types of LDNM coatings are possible, as well as various thin-film, dispersed and composite nanomaterials based on them.

In the principle, it is possible to realize the self-organized synthesis of this kind coating from the vapor phase or the atomic beam, for example, the synthesis of metal LDNM coatings on the surface of a single-crystal silicon substrate.

Previously, we called LDNM coating of metal on silicon by multilayer non-bulk (or surface) phase[12], thin-film or 2D nanophase[13,14]. Then, we gave them the general name "ν-phases" due to their undetermined structure. Each of these titles reflects only single look at the structure of LDNM coatings. This is due to the complicated structure of the LDNM coatings and difficulty of its structure identification from experimental data.

Indeed, the existing diversity of experimental methods of investigation (X-ray, electron, ion, probe microscopies and spectroscopies) are well developed for studying a single-crystaline or amorphous state of a homogeneous massive or thin (ultrathin) film. But, in the case of an inhomogeneous, nanophase or low-dimensional disordered or partially ordered structure of phase, most of these methods give little information about its structure. The method of electron spectroscopy of the characteristic loss of electron energy (EELS) at low primary beam energy has made it possible to reveal the integral structure of the ν-phase.

The energy position of the peak of plasmon losses in the EELS spectrum gives information on the frequency of the plasma oscillations of the valence electrons. And it, in turn, gives information on the density of atoms with a determined amount of valence electrons or the density of valence electrons of these atoms. For the solid, an approximation of hard balls works usually, in which atoms are packed very tightly one with other like hard balls. But, in general, it is possible to violate the strictly ordered and densest structure of atomic packing. It can be made by inserting vacancies, by rotating the bonds, inserting the intercluster interfaces and rotating the clusters themselves relative to each other. In general, this leads to the fact that the atoms are not closely connected to each other and, in general, their packing will not be tight[10].

In the case of such packing faults, for example, in the case of the ν-phase, not one peak of bulk plasmon losses (BPL) is formed in the EELS spectrum, but a whole group of peaks. Each peak in this group corresponds to a local collective interaction between electrons of one type of configuration of interatomic bonds with the same electron density. This leads to the fact that the BPL-peak shifts, expands and decreases in intensity. Thus, by the shift, the degree of expansion of the BPL-peak and the decrease in its intensity are possible to identify the type of nano-coating, for example, to distinguish between a bulk nano-coating and a ν-phase and the thickness range at which it is formed.

Indeed, a series of experiments on studying the initial stage of growth of transition metals on silicon by EELS spectroscopy show the formation of the LDNM coatings, which are, in a sense, a nanophase wetting layers.

Figure 1 and **Figure 2** present families of EELS spectra, showing changes in the formation of interfaces of Fe with Si (001) and Cr with Si (111), respectively. **Figure 1(a)** illustrates the initial stages of Fe growth on silicon with Fe-Si intermixing. **Figure 1(b)** illustrates the initial stages of growth of pure Fe. And **Figure 1(c)** illustrates the growth of Fe-Si phases after annealing films on **Figure 1(b)**.

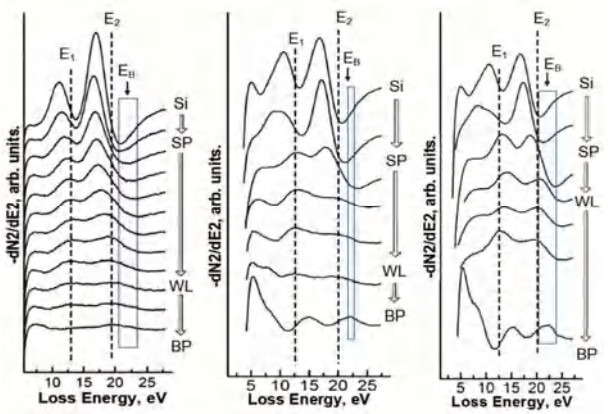

Figure 1. (a) and **(b)** – EELS of Fe on Si (001) at the initial stages of Fe growth with **(a)** and without **(b)** Fe-Si intermixing; **(c)**-the growth of Fe-Si phases on Si (001) after middle temperature (250ºC) annealing of pure Fe films[15].

In each case, we see transitions:

1) From a substrate of pure silicon (Si) to the surface phase (SP);

2) From SP to the wetting layer (WL);

3) From WL of maximum thickness to the bulk phase (BP) of the metal or the metal-silicon compound (silicide).

These transitions show position changes of the peak of surface (E1) and bulk (E2) losses and position (EB) of the peak of bulk losses in BPs.

It can be seen from **Figure 1**, that at a certain thickness, a nonmonotonic (more sharp) increase in the energy of the peak of the volume plasmon losses is observed. This increase indicates the transition from WL (v-phase) to BP of Fe or to BP of Fe silicide. And this, in turn, proves that the formation of a WL (v-phase) under non-equilibrium conditions (deposition at room temperature) in the silicon-metal-substrate system is the general pattern of the formation of the metal-silicon interface.

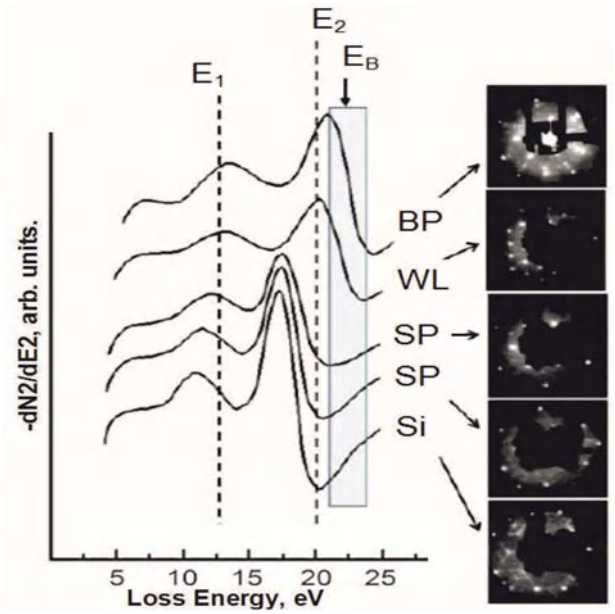

Figure 2. EELS and LEED of ordered (epitaxial) phases of Cr-Si on Si(111) at the initial stages of Cr growth (with Cr-Si intermixed) after high temperature (400-550ºC) annealing[15].

As is shown in **Figure 2**, under the solid-phase epitaxy of WL, after formation of surface phases, even its ordering occurs. At the same time, the atomic density of the WL turns out to be very close to the density of the bulk silicide, unlike the atomic densities of the preceding surface phases, which are close to the density of the silicon substrate.

2.4 Properties and applications of low-dimensional nano-coatings

Due to the low thickness of the LDNM-coatings and the vacuum environment for vapor-phase physical deposition, the sphere of application of LDNM-coatings is limited by the element base of electronics, optoelectronics and telecommunications. In addition, they can be used for various specialized applications where there are no mechanical damages, the influence of the corrosive environment and the atmosphere (mainly sensors).

At the same time, a cluster or atomic/nanoscale structure, non-uniform along the plane and an atomic/nanoscale gradient of structure properties in the transverse direction, determine specific properties and limit the variety of applications of the LDNM-coatings.

The examples of specific properties are primarily increased wetting ability, increased surface area, and increased curvature of the surface. Due to the reduced density, the presence of clusters, amorphousness, and a large quantity of vacancies is also a modified electronic structure. And, as a result, this is modified optical (nano-coatings with high IR reflection and UV absorption), magnetic (magnetic-soft and magnetic-hard nano-coatings) and electrical (nano-coatings with high conductivity) properties[16]. In addition, in LDNM-coatings, by analogy with multilayer coatings, the chemical potential gradient is possible and, as a consequence, built-in electric field is present.

3. Conclusion

The low-dimensional nano-coatings (with the thickness in nanometer range), which are produced by means of thermal vapor-phase deposition technologies, have been analyzed. In particular, the results of the investigation of low-dimensional nanometric wetting layers forming at the interface between the metal film and the monocrystal silicon substrate have been presented. A new type of nanophase coatings is proposed, which is low-dimensional nanometric coatings. These coatings can be used in the nanophase state, can have low-dimensional heterogeneity and can provide a number of new properties. The designing principles of the structure of proposed nano-coatings and a new approach to their building are considered. It has been proposed possible applications and properties of low-dimensional nanometric coatings.

References

1. Hannink RHJ, Hill AJ (editors). Nanostructure control of materials. Cambridge: Woodhead Publishing Limited; 2006. p. 368.
2. Voorhoeve RJH. Molecular beam deposition of solids on surfaces: Ultrathin films. In: Treatise on Solid State Chemistry. Boston, MA: Springer; 1976. p. 241–342.
3. O'Connor DJ, Sexton BA, Smart RSC (editors). Surface analysis methods in material science. New York/Berlin: Springer Verlag; 1992. p. 480.
4. Katayama M, Lifshits VG, Saranin AA, *et al*. Surface science. An introduction. Berlin: Spriner-Verlag; 2003. p. 440.
5. Henini M (editor). Molecular beam epitaxy: from research to mass production. London: Elsevier; 2012. p. 744.
6. Plyusnin NI, Il'yashchenko VM, Krylov SV, *et al*. Effect of incident atomic beam power on the formation of a Fe/Si(111)7×7 interface. Technical Physics Letters 2007; 33: 486–489.
7. Plusnin NI. Atomic-scale control of molecular-beam growth of nanolayers. In: Comprehensive Guide for Nanocoatings Technology, Characterization and Reliability. New York: Nova Science Publishers Inc.; 2015. p. 87–101.
8. Plyusnin NI, Tarima NA, Il'yashchenko VM, *et al*. The effect of underlayer-modified atomic monolayer on the mechanism of subsequent film growth. Technical Physics Letters 2012; 38: 324–327.
9. Plusnin NI. Application of AES and EELS for surface/interface characterization. Journal of Electron Spectroscopy and Related Phenom 2004; 137-140: 161–164.
10. Plusnin NI. The use of AES and EELS for complex analysis of two-dimensional coatings and their growth process. Modern Electronic Materials 2017; 3(4): 131–141.
11. Plyusnin NI. From physics of the interface formation to low–dimensional nanocoatings and nanomaterials based on them. VESTNIK of Far East Branch of Russian Academy of Science 2016; 4(188): 27–35. Available from: https://cyberleninka.ru/article/n/ot-fizki-formirovaniya-granitsy-razdela-k-nizkorazmernym-nanopokrytiyam-i-materialam-na-ih-osnove.
12. Plusnin NI, Galkin NG, Lifshits VG, *et al*. Formation of interfaces and templates in the Si(111)-Cr system. Surface Review and Letters 1995; 2(4): 439–449.
13. Plusnin NI, Il'iashchenko VM, Kitan' SA, *et al*. Metal thin-film nanophases and their interface with silicon. Journal of Physics: Conference Series 2008; 100(5).
14. Plyusnin NI, Il'yashchenko VM, Kitan' SA, *et al*. Formation, electronic structure, and stability of film nanophases of transition metals on silicon. Journal of Surface Investigation. X-Ray, Synchrotron and Neutron Techniques 2009; 3(5): 734–746.
15. Plyusnin NI. Atomic-scale AES-EELS analysis of structure-phase state and growth mechanism of layered nanostructures. Advances in Materials Physics and Chemistry 2016; 6(7): 195–210.
16. Plyusnin NI. Metallic nanofilms on single crystal silicon: Growth, properties and applications. Modern Electronic Materials 2017; 3(2): 57–65.

Characterization and Application of Nanomaterials (2019) Volume 2 Issue 2
doi:10.24294/can.v2i2.791

REVIEW ARTICLE

Synthesis and characterization methods of polymeric nanoparticles

Aslı Katmıs, Serap Fide, Seyma Karaismailoglu, Serap Derman*

Chemical and Metallurgy Faculty, Bioengineering Department, Yildiz Technical University 34220, Istanbu, Turkey.
E-mail: serapacar5@gmail.com

ABSTRACT

This review provided a detailed overview of the different synthesis and characterization methods of polymeric nanoparticles. Nanoparticles are defined as solid and colloidal particles of macromolecular substances ranging in size under 100 nm. Different types of nanoparticles are used in many biological fields (bio-sensing, biological separation, molecular imaging, anticancer therapy, etc.). The new features and functions provided by nano dimensions are largely different from their bulk forms. High volume/surface ratio, improved resolution and multifunctional capability make these materials gain many new features.

Keywords: Nanoparticle; Polymer; Synthesis Methods; Characterization Methods; Particle Size

ARTICLE INFO

Article history:
Received 2 July 2019
Received in revised form 28 July 2019
Accepted 1 August 2019
Available online 14 August 2019

1. Introduction

Nanoparticles are defined as solid and colloidal particles of macromolecular substances ranging in size under 100 nm[1,2]. There are different application fields that led to the exploration of different nano compositions. For instance, they are able to polymerize NPs, biological NPs, lipid-based NPs and metal-based NPs[3-6]. Biocompatible and biodegradable polymers are used for preparation of the polymeric nanoparticles. Polymers are used as biomaterials because of their useful properties such as good biocompatibility, biodegradability, easy preparation and design, various chemical structures and interesting biological imitation character[7].

Most polymeric NPs are biodegradability and biocompatible, and over the accomplished few decades, researches had accepted sample absorption in developing biodegradable NPs as a drug-delivery system[8]. These biodegradable polymeric nanoparticles coated with hydrophilic polymers known as long period of time circulating particles, have been used as potential drug delivery vehicles for their ability to control drug release for a long time. Polymeric nanoparticles have the ability to deliver drugs, proteins, peptides, and antigens and they can be targeted to particular organ. Additionally, they can be used as DNA transporters in gene therapy[9-11].

There are many biodegradable polymers that can be produced from proteins such as milk proteins and gelatin; polysaccharides such as starch, chitosan and sodium alginate; and synthetic polymers such as polymethylmethacrylate, poly (cyanoacrylate) PCA, poly-ε-caprolactone (PCL), poly (lactic acid) (PLA), poly (D, L-glycolic acid) (PGA), and their copolymer of poly (lactide-co-glycolide) PLGA are used in preparing nanoparticular systems[12]. Nanoparticles which ob-

tained by using natural or synthetic polymers have two major advantages for targeting of proteins, peptides and genes, as well as drugs.

The first property is that the nanoparticles have small particle sizes. In this way, they pass more easily than small capillaries, which are easier to enter intracellular and extracellular spaces[13], and release effective active substance in the target region[14,15].

The second property is to use biodegradable materials in the preparation of nanoparticles. Biodegradable materials provide controlled release of active substance in the target tissue for days to further weeks.

In addition, nanoparticles have a good deal of advantages that can be:

1) Nanoparticles have a protective effect against the enzymatic degradation of active substances such as drugs, proteins or peptides in the biological system. They can also increase their stability while reducing side effects[13,14].

2) Beside this, drugs can be encapsulated to the nanoparticle systems without any chemical reaction; this is important for protecting the biological activity of drug[9].

3) Site-specific targeting of nanoparticles can be accomplished by adhering targeting ligands to particles surface or use of magnetic guidance[9].

4) They allow rapid-formulation development. The nanoparticle systems can be used for different routes of administration including oral, parenteral, intra-ocular, nasal etc.[9].

2. Preparation methods of polymeric nanoparticles

Polymeric nanoparticles can be prepared by dispersing performed polymers, using different methods such as solvent evaporation, nanoprecipitation, salting-out, dialysis and supercritical fluid technology.

These methods have similar properties that they involve an organic phase containing the nanoparticle components and a water phase containing stabilizers. The other similarity is the poor encapsulation efficiency of partially water soluble and freely water-soluble drugs (involving proteins and peptides), which escape from the organic phase to the aqueous phase[16].

2.1 Solvent evaporation

The most widely used method to prepare the polymeric nanoparticles for the delivery of active substance is solvent evaporation[17]. This method is used for producing polymeric nanoparticles by biodegradable polymers which have been applied in the drug delivery systems. In this method, the polymer and drug are dissolved in an organic solvent and emulsions are formulated using the aqueous solution of surfactants. In the past, dichloromethane or chloroform were used as the solvent for dissolving the hydrophobic drug. But now, ethyl acetate is used instead of dichloromethane and chloroform because of their toxicological profile[9,17].

Solvent evaporation method has two main strategies that are used for the formation of emulsions. The first one is the preparation of single-emulsions [(oil-in-water, (o/w)], and the second one is dou-ble-emulsions [(water-in-oil-in-water, (w/o/ w)].

In this method, high-speed homogenization or ultra-sonication are used for preparation of emulsion. After that, the organic solvent is evaporated and the nanoparticles are collected by ultracentrifugation. For removing of surfactants, the nanoparticles are washed with distilled water. Nanoparticles can be lyophilized after all steps.

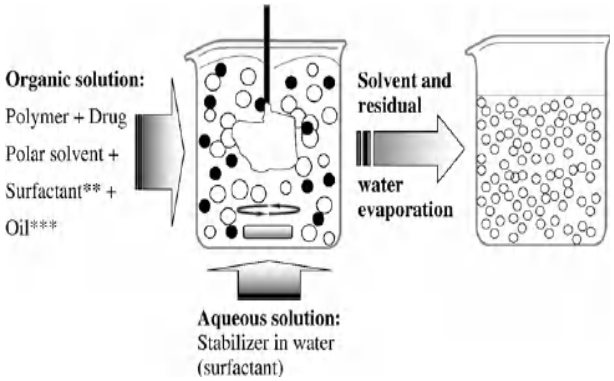

Figure 1. Schematic representation of the solvent-evaporation method[18].

While solvent evaporation method (**Figure 1**) is a simple method for the preparation of polymeric nanoparticles, it is needed to the external energy. The power of external energy, time consuming and pos-sible agglomeration of the nanodroplets, during the evaporation process, may affect the particle size and morphology of nanoparticles[17].

2.2 Salting out

Salting out is another method for preparation of polymeric nanoparticles (**Figure 2**). This method is based on the separation of a water miscible solvent as acetone by using salting out effect. In other words, salting out technique is a modification of the emulsification/solvent diffusion by beginning with an emulsion[19,20]. The organic phase is prepared by dissolving the polymer in a solvent that is totally miscible in water such as acetone, tetrahydrofuran and ethanol. Then, this organic phase is added to the aqueous phase that is constituted by water, the salting-out agent and a stabilizer. The choice of salting out agent that can be electrolytes, such as calcium chloride, magnesium chloride or non-electrolytes, such as sucrose, which is so important for encapsulation efficiency of drug. In the following procedure, an sufficient volume of water is added to the mixture and the resulting nanoparticles are collected via cross-flow filtration[20].

Salting out method has some advantages, of which the most important is reducing stress to protein encapsulants. Another advantage is that it does not lead to an increase of temperature. Therefore, heat sensitive molecules can be processed by this method. On the contrary, this method has some disadvantages that lie in specific application to lipophilic drugs and extensive washing steps[19].

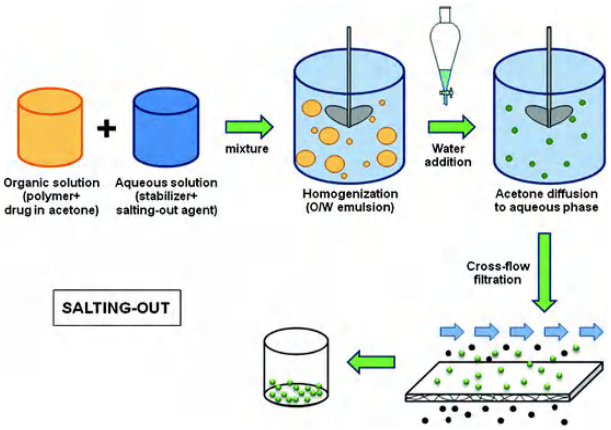

Figure 2. Schematic representation of the salting-out method[20].

2.3 Nanoprecipitation

This method is also called solvent displacement (**Figure 3**), which is a simple, rapid and reproducible method largely used for the preparation of nanocapsules and nanosphere, besides the meaning of solvent displacement[17,21,22].

The basic principle is the interfacial collapse of the substitutional polymer of the splitting solvent which can be miscible with the water in the lipophilic solution. The polymer (synthetic, semi synthetic, or natural), organic solvent of the polymer and the water (non-solvent for the polymer) are three basic components of nanoprecipitation system. Organic solvent should be miscible in water and easy to remove by evaporation. Thus, in the nanoprecipitation method, acetone is the most widely used solvent. Nanoprecipitation occurs when the polymer solution is added to the non-solvent[22].

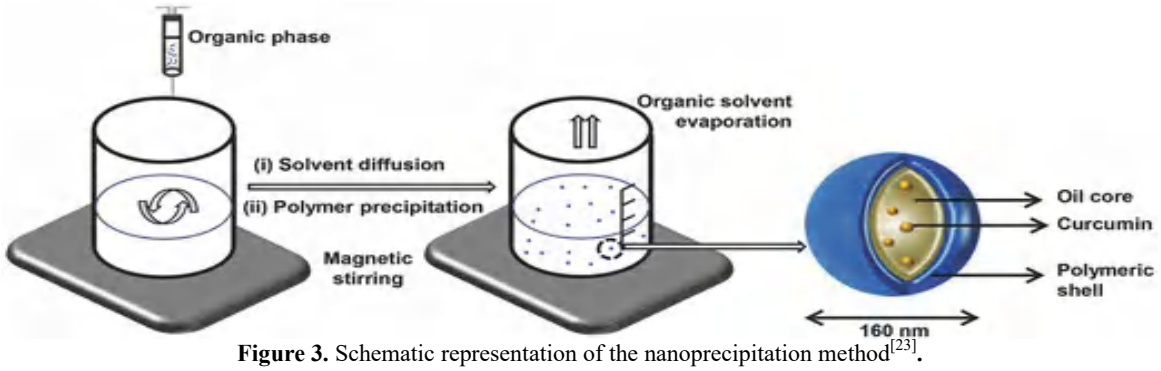

Figure 3. Schematic representation of the nanoprecipitation method[23].

2.4 Dialysis

Dialysis is a preparation method that provides a basic and effective way to prepare small PNPs (**Figure 4**).

Firstly, the polymer is dissolved in the organic solvent and then put inside a dialysis tube while producing the nanoparticle by dialysis. It is an important point that the dialysis tube is suitable for the molecular weight of the nanoparticle. During dialysis, the solvent loses its solubility as a result of displacement. In this way, progressive aggregation of the polymer occurs and a homogeneous suspension

of nanoparticles is obtained[14,17].

2.5 Super critical fluid technology

Supercritical fluids are generally defined as fluids that do not change in phase despite the change of pressure (**Figure 5**). Supercritical CO_2, which is the most widely used supercritical fluid, because it is compatible with the critical state (Tc = 31.1°C, Pc = 73.8 bar), is nontoxic, nonflammable, and inexpensive[15,24].

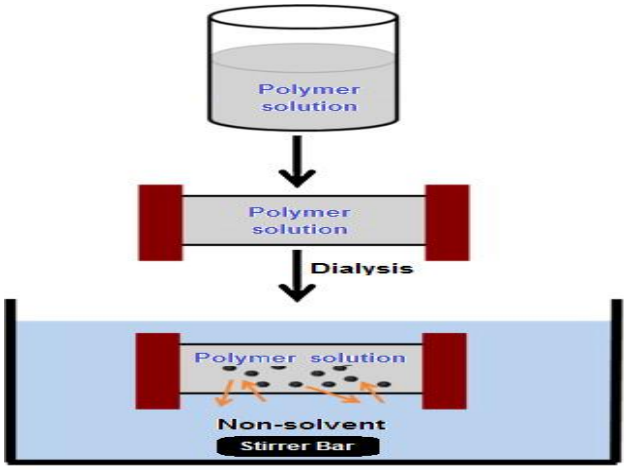

Figure 4. Schematic representation of dialysis method[17].

Supercritical fluid technology is expected to offer an interesting and effective particle production technique, avoiding many of the disadvantages of traditional methods[17]. The greatest advantage of the supercritical fluid technology method used to prepare polymeric nanoparticles is that the precipitated product does not contain solvent[15,24].

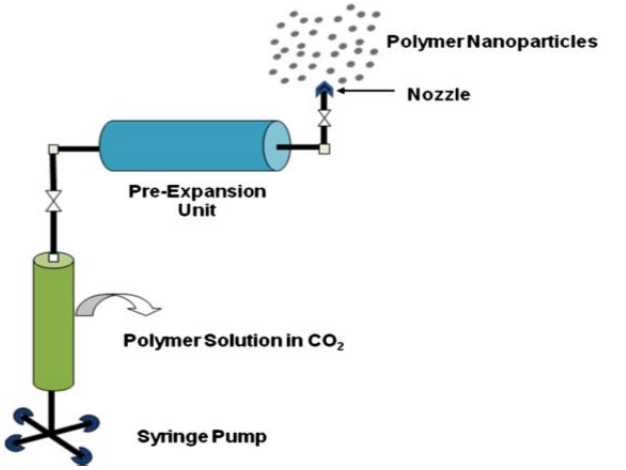

Figure 5. Schematic representation of super critical fluid technology method[17].

The most widely used methods are rapid expansion of supercritical solution (RESS) and supercritical anti-solvent method (SAS). In the RESS method, the drug substance is dissolved in the organic solvent and then released to the supercritical fluid. The organic phase rapidly dissolves in the supercritical solvent and remains nanoparticles that can be filtered back. In the SAS method, the active substance and polymer are dissolved in the supercritical solvent at high pressure[25,26].

2.6 Mini-emulsion

Mini-emulsion polymerization is based on a typical formulation of water, a monomer mixture, surfactant, co-stabilizer and initiator. It is used of a low molecular weight co-stabilizer compound in this method. Mini-emulsions are critically balanced. Also, it requires high-shear stress to achieve a steady state, and interface strain is much bigger than zero[19].

3. Characterization methods of polymeric nanoparticles

Characterization of nanoparticles is based on analysis of particle size, zeta potential, polydispersity index (PDI), morphology, surface area and composition. The most important characteristics of na- noparticles are particle size and size distribution which can influence drug loading, drug release, and stability of nanoparticles (**Figure 6**). The other important characteristic of nanoparticles is zeta potential that is used to characterize the surface charge property[1].

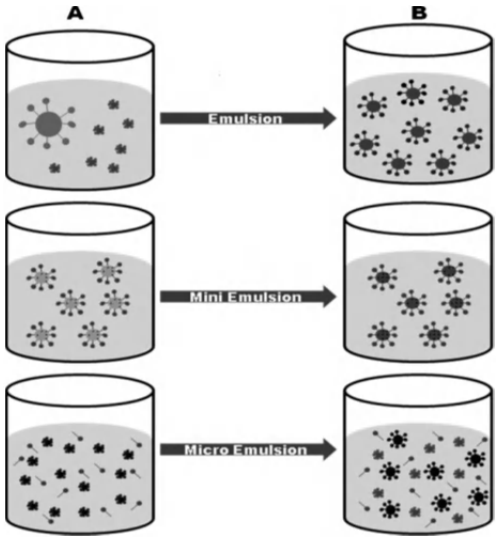

Figure 6. (A) Differences among various hetero-phase polymerization methods before and **(B)** after polymerization[17].

There are some advanced microscopic techni-

ques such as atomic force microscopy (AFM), scanning electron microscopy (SEM) and transmission electron microscopy (TEM), which are used for characterization of nanoparticles. Laser light scattering (LLS), especially dynamic light scattering (DLS) is used for measurement of size and size distribution; Atomic force microscopy (AFM) and scanning electron microscopy (SEM) are used for morphological studies; X-Ray photoelectron spectroscopy (XPS) is used for surface chemistry analysis of nanoparticle suspension[1].

3.1 Transmission electron microscopy (TEM)

Transmission electron microscopy is a useful technique for the investigation shape and size of nanoparticles. In other words, imaging, diffraction and spectroscopic information can be provided by TEM. TEM and SEM give the same kind of information despite different study principles. Sample preparation for the TEM is complicated and time-consuming due to the need to be very thin sample for electron affinity. Nanoparticle sample is precipitated in the films during TEM characterization, and then immobilized with staining material. This process provides withstanding against vacuum. At the point, when an electron bar is transmitted through an ultra-fine, it contacts with the sample and the surface characteristics of the sample are obtained[27].

3.2 Scanning electron microscopy (SEM)

Scanning electron microscopy works on the principle of scanning the surface with high-energy electrons that focus on a very small area. Especially it is based on the principle of creating images by reflecting electrons from the sample. SEM has some advantages in morphological and dimensional analysis, it gives limited information about size distribution and actual population averages[28].

Electrons produced by an electron gun are accelerated by an anode and are made parallel to each other by magnetic lenses. Thus, the electron beam to be used for the measurement is prepared. For this purpose, the electron beam that focused by the objective lens and is picked up by the condenser electromagnetic lens performs the scanning process on the sample surface by the electromagnetic deflector coils[29].

3.3 Atomic force microscopy (AFM)

The AFM creates an image based on the surface forces that occur between the sample surface and the tip attached to an arm. The sharp tip used in this technique is 1-2 microns long and less than 100 Å in diameter. The forces that occur between the surface of material and the tip that are inspected during a probe travel cause to diverge the position of the tip. The surface topography is created by measuring this deviation. Atomic force microscope can be operated with 3 different ways.

The first of these is called the “contact” type. In this method, the sharp tip makes soft physical contact with the surface and the changes that are happening in the position of the arm are recorded. In the “non-contact” type, the arm vibrates in a position close to the sample surface (50-150 Å). In this method, the attractive Van der Waals forces acting and depending on the changes in the surface and the changes occurring in the frequency of the vibration of the arm are measured. The final “tapping” method is similar to the method of contact. This potent technique allows high resolution topographic imaging of sample surfaces[30-32].

3.4 X-Ray diffraction (XRD)

X-ray diffraction (XRD) is an important technique used in crystal structure determination of nanoparticles. In this technique, the types of atoms at lattice point, crystal planes and plane distances can be determined without damaging the sample. Different diffraction patterns occur depending on the structure of the crystal and the wavelength of the light interacting with the crystal. The diffraction occurs as a result of the interference of reflected rays from different layers of the material in the periodic structure. The condition for the occurrence of the diffraction is given by the Law of Bragg[33,34].

3.5 Fourier transform infrared spectroscopy (FT-IR)

The Fourier transform infrared spectroscopy is used for the chemical functional group analysis on the surface of nanoparticles. IR radiation is sent onto the sample in the Fourier transform infrared spectroscopy (FT-IR). While some of this radiation is

absorbed by the sample, some of it also passes and thus, absorption and transmission spectra of the molecules come out. These absorption/transmission spectra are the characteristic spectra of the molecules in the sample and define the absorption/transmission peaks of the material. These peaks correspond to the vibrational frequencies of the bonds between the atoms in the material. The intensity of the peaks gives information about the amount of the material as well as the wavelengths at which the peaks appear in the spectrum to define the bonds between the atoms. For this reason, FT-IR spectroscopy is a useful method to characterize the material[33,35].

3.6 Dynamic light spectroscopy (DLS)

Dynamic light spectroscopy (DLS) or other known photon correlation spectroscopy is used to determine particle size distribution and particle size characterization. DLS calculates the size of the nanoparticle in a solvent based on the Brownian motion. The hydrodynamic diameter of the diffusion factor in a homogeneous solution is determined by Stokes Einstein equation. DLS measurement is suitable for monodisperse and polydisperse materials, but DLS measurement is not suitable for high-dimensional samples. In addition, large size samples are dispersed in a solvent for measurement. DLS has the most common and fairly simple measuring technique thanks to its large measuring range[29]. The main advantage of the DLS technique is that measurements can be made in a short time and the cost of the apparatus is low[36].

3.7 Electrophoretic light scattering

Electrophoretic light scattering (ELS), is by far the best methods for zeta potential determination of suspended particles, due to its sensitivity, accuracy, and versatility[37]. Particles contained in aqueous colloidal solutions carry electrical charge. Zeta potential is varying depending on the nature of the material and the environment e.g., pH, ionic strength, and even the type of ions in the particle suspension. The most important mechanisms of surface charge are ionization of surface groups, dissolution and adsorption of charged species.

Zeta potential measurements are based on the "electrophoresis" technique. Accordingly, when an electric field is applied to the liquid phase, the charged particles suspended in the liquid move toward the charged electrode opposite to their own charge. The viscous forces that acting on the particle try to prevent this movement. When the two opposing forces are balanced, the particles move at a constant speed. This speed depends on the following factors:

1) The power of the electric field;
2) The dielectric constant of the medium;
3) Viscosity of the medium;
4) Zeta potential;

The value of the zeta potential also provides information about the stability of the colloidal solution. The stability of colloidal particles varies with the type and rate of interaction between the particles. If all the particles in the suspension have a large negative or positive zeta potential, they push each other, agglomeration or precipitation will not occur. When the zeta potential is low, there is not enough force to keep the particles away from each other and agglomeration occurs. This value is accepted as +/- 30mV[30, 38].

References

1. Singh R, Lillard Jr JW. Nanoparticle-based targeted drug delivery. Experimental and Molecular Pathology 2009; 86(3): 215–223.
2. Khan I, Saeed K, Khan I. Nanoparticles: Properties, applications and toxicities. Arabian Journal of Chemistry 2017; 12(7): 908–931.
3. Dash TK, Konkimalla VB. Poly-caprolactone based formulations for drug delivery and tissue engineering: A review. Journal of Controlled Release Society 2012; 158(1): 15–33.
4. Szot CS, Buchanan CF, Gatenholm P, *et al.* Investigation of cancer cell behavior on nanofibrous scaffolds. Materials Science and Engineering: C 2011; 31(1): 37–42.
5. Hughes GA. Nanostructure-mediated drug delivery. Nanomedicine Nanotechnology Biology & Medicine 2005; 1(1): 22–30.
6. Faraji AH, Wipf P. Nanoparticles in cellular drug delivery. Bioorganic & Medicinal Chemistry 2009; 17(8): 2950–2962.
7. Mansour HM, Sohn MJ, Al-Ghananeem A, *et al.* Materials for pharmaceutical dosage forms: Molecular pharmaceutics and controlled release drug delivery aspects. International Journal of Molecular Sciences 2010; 11(9): 3298–3322.
8. Parveen S, Misra R, Sahoo SK. Nanoparticles: A boon to drug delivery, therapeutics, diagnostics and imaging. Nanomedicine: Nanotechnology, Biology and Medicine 2012; 8(2): 147–166.

9. Mohanraj V, Chen Y. Nanoparticles: A review. Tropical Journal of Pharmaceutical Research 2006; 5(1): 561–573.
10. Langer R. Biomaterials in drug delivery and tissue engineering: one laboratory's experience. Accounts of Chemical Research 2000; 33(2): 94–101.
11. Lee M, Kim SW. Polyethylene glycol-conjugated copolymers for plasmid DNA delivery. Pharmaceutical Research 2005; 22(1): 1–10.
12. Esfanjani AF, Jafari SM. Biopolymer nano-particles and natural nano-carriers for nano-encapsulation of phenolic compounds. Colloids and Surfaces B: Biointerfaces 2016; 146: 532–543.
13. Kashi T, Eskandarion S, Esfandyari-Manesh M, *et al*. Improved drug loading and antibacterial activity of minocycline-loaded PLGA nanoparticles prepared by solid/oil/water ion pairing method. International Journal of Nanomedicine 2012; 7: 221–234.
14. Derman S, Kizilbey K, Akadeste ZM. Polymeric nanoparticles. Sigma 2013; 31: 107–120.
15. Öztürk K. Design and evaluation of nanoparticle carrier systems containing free radical cleaner material [Master's thesis] (in Turkish). Ankara: Hacettepe University; 2010.
16. Quintanar-Guerrero D, Allémann E, Fessi H, *et al*. Preparation techniques and mechanisms of formation of biodegradable nanoparticles from preformed polymers. Drug Development and Industrial Pharmacy 1998; 24(12): 1113–1128.
17. Rao JP, Geckeler KE. Polymer nanoparticles: Preparation techniques and size-control parameters. Progress in Polymer Science 2011; 36(7): 887–913.
18. Reis CP, Neufeld RJ, Ribeiro AJ, *et al*. Nanoencapsulation I. Methods for preparation of drug-loaded polymeric nanoparticles. Nanomedicine: Nanotechnology, Biology and Medicine 2006; 2(1): 8–21.
19. Nagavarma B, Hemant KSY, Ayaz A, *et al*. Different techniques for preparation of polymeric nanoparticles — A review. Asian Journal of Pharmaceutical and Clinic Research 2012; 5(3): 16–23.
20. Fonseca AC, Ferreira P, Cordeiro RA, *et al*. Drug delivery systems for predictive medicine: polymers as tools for advanced applications. In: New strategies to advance pre/diabetes care: Integrative approach by PPPM. Springer; 2013. p. 399–455.
21. Mishra B, Patel BB, Tiwari S. Colloidal nanocarriers: A review on formulation technology, types and applications toward targeted drug delivery. Nanomedicine: Nanotechnology, Biology and Medicine 2010; 6(1): 9–24.
22. Bilati U, Allémann E, Doelker E. Development of a nanoprecipitation method intended for the entrapment of hydrophilic drugs into nanoparticles. European Journal of Pharmaceutical Sciences 2005; 24 (1): 67–75.
23. Klippstein R, Wang JTW, Riham I, *et al*. Passively targeted curcumin-loaded PEGylated PLGA nanocapsules for colon cancer therapy in vivo. Small 2015; 11(36): 4704–4722.
24. Sun Y, Meziani MJ, Pathak P, *et al*. Polymeric nanoparticles from rapid expansion of supercritical fluid solution. Chemistry-A European Journal 2005; 11(5): 1366–1373.
25. Thote AJ, Gupta RB. Formation of nanoparticles of a hydrophilic drug using supercritical carbon dioxide and microencapsulation for sustained release. Nanomedicine: Nanotechnology, Biology and Medicine 2005; 1(1): 85–90.
26. Özcan İ. Design and evaluation of in vitro-in vivo nanoparticle drug-ing systems prepared using biodegradable polymers synthesized to target bone [Master's thesis] (In Turkish). Izmir: Ege University; 2008.
27. Molpeceres J, Aberturas M, Guzman M. Biodegradable nanoparticles as a delivery system for cyclosporine: Preparation and characterization. Journal of Microencapsulation 2000; 17(5): 599–614.
28. Zhou W, Wang Z. Scanning microscopy for nanotechnology: Techniques and applications. Springer; 2007.
29. Şimsek UB. Zero value iron nanoparticle production, optimization and use of textile dyeing under different synthesis conditions [Master's thesis] (In Turkish). Mersin: Mersin University; 2015. p. 131.
30. Tokay B, Erdem Şenatalar A. Investigation of the mechanism of silicate-1 synthesis from nanotanes (in Turkish). ITU Dergisi D 2011; 7(5).
31. Li H. Atomic force microscopy [Internet]. 1997 [updated 1997 April 24] Available from: http://www.Cheimstry.uoguelph.ca/educmat/chm729/afm/firstpag.htm
32. Cohen SH, Bray MT, Lightbody ML. Atomic force microscopy/scanning tunneling microscopy. New York, London: Plenum Press; 2002.
33. Karaağaç Ö. Synthesis, characterization and enzyme immobilization application of superparamagnetic nanoparticles with optimum saturation magnetiza-tion [Master's thesis] (in Turkish). Balikesir: Balikesir University; 2007-2011.
34 Cullity BD, Stock SR. Elements of X-ray diffraction. New York: Prentice-Hall; 2001.
35. Skoog DA, Holler FJ, Nieman TA. Principles of instrumental analysis. Toronto: Thomson Learning. Inc.; 1998.
36. Bootz A, Vogel V, Schubert D, *et al*. Comparison of scanning electron microscopy, dynamic light scattering and analytical ultracentrifugation for the sizing of poly (butyl cyanoacrylate) nanoparticles. European Journal of Pharmaceutics and Biopharmaceutics 2004; 57(2): 369–375.
37. Xu R. Progress in nanoparticles characterization: Sizing and zeta potential measurement. Particuology 2008; 6(2): 112–115.
38. Clogston JD, Patri AK. Zeta potential measurement. In: Characterization of nanoparticles intended for drug delivery. Springer; 2011.p. 63–70.

Characterization and Application of Nanomaterials (2019) Volume 2 Issue 2
doi:10.24294/can.v2i2.813

REVIEW ARTICLE

Interaction of light with lead halide perovskites: A review

Zhiya Dang*, Duc Anh Dinh

Nanochemistry Department, Istituto Italiano di Tecnologia, via Morego 30, 16163 Genova, Italy. E-mail: rongmeijiao yin@gmail.com

ABSTRACT

Lead halide perovskites are the new rising generation of semiconductor materials due to their unique optical and electrical properties. The investigation of the interaction of halide perovskites and light is a key issue not only for understanding their photophysics but also for practical applications. Hence, tremendous efforts have been devoted to this topic and brunch into two: (i) decomposition of the halide perovskites thin films under light illumination; and (ii) influence of light soaking on their photoluminescence (PL) properties. In this review, we for the first time thoroughly compare the illumination conditions and the sample environment to correlate the PL changes and decomposition of perovskite under light illumination. In the case of vacuum and dry nitrogen, PL of the halide perovskite ($MAPbI_{3-x}Cl_x$, $MAPbBr_{3-x}Cl_x$, $MAPbI_3$) thin films decreases due to the defects induced by light illumination, and under high excitations, the thin film even decomposes. In the presence of oxygen or moisture, light induces the PL enhancement of halide perovskite ($MAPbI_3$) thin films at low light illumination, while increasing the excitation, which causes the PL to quench and perovskite thin film to decompose. In the case of mixed halide perovskite ($(MA)Pb(Br_xI_{1-x})_3$) light induces reversible segregation of Br domains and I domains.

Keywords: Lead Halide Perovskites; Light Illumination; Photoluminescence; Decomposition; Segregation

ARTICLE INFO

Article history:
Received 9 October 2019
Received in revised form 2 November 2019
Accepted 5 November 2019
Available online 19 November 2019

1. Introduction

Lead halide perovskites (LHPs), with the chemical formula of $APbX_3$ (A = Cs, CH_3NH_3 (MA), $CH(NH_2)_2$ (FA), X = Cl, Br, I), have emerged as the new generation of intriguing semiconductor materials for solar cells[1-4], lasers[5,6], light emitting diodes[3,5], and photodetectors[7,8] in recent years. The rapid development of LHPs in these fields arises from the ease of processability, as well as their unique optical and electrical properties, such as small exciton binding energy, long exciton diffusion lengths, low charge recombination, high absorption coefficient, a direct bandgap and its tunability over near-infrared, visible to ultraviolet range[9-15]. One of the major obstacles hindering the industrialization of LHPs is the toxicity of lead (Pb), for which lead-free halide perovskites have been widely explored to replace Pb with non-toxic metals, such as Mn(II), Sn(II), Sn(IV), Bi(III), Sb(III), Cu(II) etc.[16-22]. Another important issue is the instability of LHPs upon exposure to the polar solvents and ambient atmospheric conditions (heat, moisture, oxygen), or radiations, such as electron and X-ray beams, originating from the low energy barrier for the halide perovskite crystal formation, and till now this still remain as a critical issue in various applications[23-30]. The LHPs degrade via different paths under the above mentioned conditions. In the presence of moisture, the degradation path of $MAPbI_3$ films as well as single crystals is initiated by for-

mation of hydrated intermediates, e.g., both monohydrate $CH_3NH_3PbI_3 \cdot H_2O$ and dihydrate $(CH_3NH_3)_4PbI_6 \cdot 2H_2O$, and the reaction can be described by the reversible chemical equations of:

$4CH_3NH_3PbI_3 + 4H_2O \leftrightarrow 4[CH_3PbI_3 \bullet H_2O] \leftrightarrow (CH_3NH_3)_4PbI_6 \bullet 2H_2O + 3PbI_2 + 2H_2O$[24,31,32]

The $MAPbCl_3$, $MAPbBr_3$ and $MAPbI_3$ are found to decompose into PbX_2, gaseous methylamine CH_3NH_2 and HX, when they are heated under low-temperature (25-150°C)[33,34]. In the case of low energy electron beam irradiation of $MAPbI_3$ thin film (4.5 to 60 eV), the material degrades with the reaction described by:

$CH_3NH_3PbI_3 \xrightarrow{e^- \rightarrow C-N\ breakage} (-CH_2-) + NH_3 + HI + PbI_2$[35]

While for $CsPbX_3$ nanocrystals in a TEM (80/200KeV), through a radiolysis process, Pb^{2+} ions are reduced to metallic Pb atoms along with the oxidation and desorption of halogen species in the vacuum. The Pb atoms further aggregate to form Pb nanoparticles at higher temperatures (above-40°C) while below -40°C the perovskites decompose into CsX, PbX_2 and CsPb domains and further halogen desorption eventually leads to only Cs and Pb species[27,28,36]. Under other types of radiations such as X-ray, halogen loss and reduction of Pb are also found to occur[27,29].

Not only unstable in moisture, oxygen, heat or radiation conditions, the LHPs are also sensitive under light[26,37,38]. Doomed to interplay with light, the investigation of interaction of halide perovskites and light is a key issue for understanding their photophysics and for characterization and practical applications, because the optical characterization techniques such as photoluminescence and absorption measurements as well as working of perovskite based devices such as solar cell, LEDs, lasers, and photodetectors, involve the interaction of halide perovskites with light. The LHPs are fabricated and applied in several forms, e.g., polycrystalline thin film with micron-size domains (mainly for organic-inorganic type $MAPbX_3$), single crystals (also for MA-PbX_3), and nanocrystals (available for all cation types $CsPbX_3$, $MAPbX_3$, $FAPbX_3$). A large amount of literatures report the decomposition of $MAPbX_3$ perovskite thin films and single crystals upon light illumination[39-41]. On the other hand, light is found to cause enhancement and quenching of photoluminescence (PL) of $MAPbX_3$ perovskite film[42-44]. Moreover, an unusual light-induced effect, photo-induced halide segregation is also reported in $(MA)Pb(Br_xI_{1-x})_3$ thin films[45-51]. In the present review, we summarize the above aspects and attempt to discuss some of the seemingly conflicting views on the interaction of perovskite and light.

2. Light illumination on halide perovskite thin films

2.1 Oxygen-free and moisture-free environment

The literatures on the light illumination effect of halide perovskite thin films in dry N_2 or vacuum are summarized in **Table 1**.

Table 1. The literatures of light illumination on halide perovskite in vacuum or dry N_2

Material	Light illumination	Environment	Film morphology	PL	Ref
$MAPbI_3$ film	405 nm laser, 0.5 W/cm^2 for 5 mins (dose: 150 J/ cm^2)	Nitrogen, vacuum	Not reported	PL decreases	[52]
$MAPbI_{3-x}Cl_x$, $MAPbBr_{3-x}Cl_x$ film	White light source, 0.0434 W/cm^2, for 24 h(89994 J/ cm^2)	Nitrogen	Almost stable	Not reported	[41]
$MAPbI_3$ film	408 nm, 0.68 W/cm^2 for 2 hours (dose: 4896 J/ cm^2)	Vacuum	Decomposition	Not reported	[40]
$MAPbI_{3-x}Cl_x$, $MAPbBr_{3-x}Cl_x$ film	White light source, 0.0434 W/cm^2, for 2 h (7499 J/ cm^2)	Vacuum	Decomposition	PL decreases	[41]
$MAPbI_3$ film	532 nm laser, 140 to 4000 W/cm^2 for Seconds (dose: 1000 to 20000 J/ cm^2)	Vacuum	Decomposition	PL decreases	[38]
$MAPbI_3$ film	470 nm laser, 0.2 to 0.9 W/cm^2 for 7 mins (84 to 378 J/ cm^2)	Encapsulated		Continuous enhancement	[44]
$MAPbI_3$ film	470 nm laser, 1.6 to 4.6 W/cm^2 for few mins (1200 J/ cm^2)	Encapsulated	may involve decomposition	Continuous quenching	[44]

Both the excitation power (W/cm^2) and dose (J/cm^2) of light matters, and an absolute comparison of these parameters cannot be made due to discrepancies in the wavelength, type of source (continu-

ous or pulsed), and fabrication method of samples. However, a rough comparison can give useful guidance on better understanding how light and perovskite interact. In nitrogen, PL of perovskite films drops over time under illumination (at power of 0.04 to 0.5W/cm^2, dose of 150 to 89994 J/cm^2) because illumination induces the defects in the $MAPbX_3$ films, yet the films are found to hardly degrade[41,52]. In vacuum, PL drops even more, and according to literatures at certain illumination conditions such as power of 0.04 to 4000 W/cm^2, dose above 1000 J/cm^2 the material is found to decompose through the following equations (1, 2)[38,40]:

$$CH_3NH_3PbI_3 \xrightarrow{light} (\text{-}CH_2\text{-}) + NH_3 + HI + PbI_2 \quad (1)$$

$$PbI_2 \xrightarrow{light} Pb + I_2 \quad (2)$$

As the above equations show the decomposition products include volatile NH_3, HI, and I_2. In nitrogen environment, the desorption of gaseous products is suppressed and therefore no obvious decomposition of the film is observed. However, in vacuum, these products are immediately desorbed which promotes the decomposition process, and the unreacted $CH_3NH_3PbI_3$, metallic Pb, and carbon hydrocarbonaceous species remain on the surface, as demonstrated by the upper row of schematics in **Figure 1A**[40]. There is a saturation of decomposition, which is about 33%, as is schematically shown by lower row of **Figure 1A**, and indicated by the change of Pb^{2+} signal and Pb^0 signal in XPS spectra at different durations of illumination in **Figure 1B**[40].

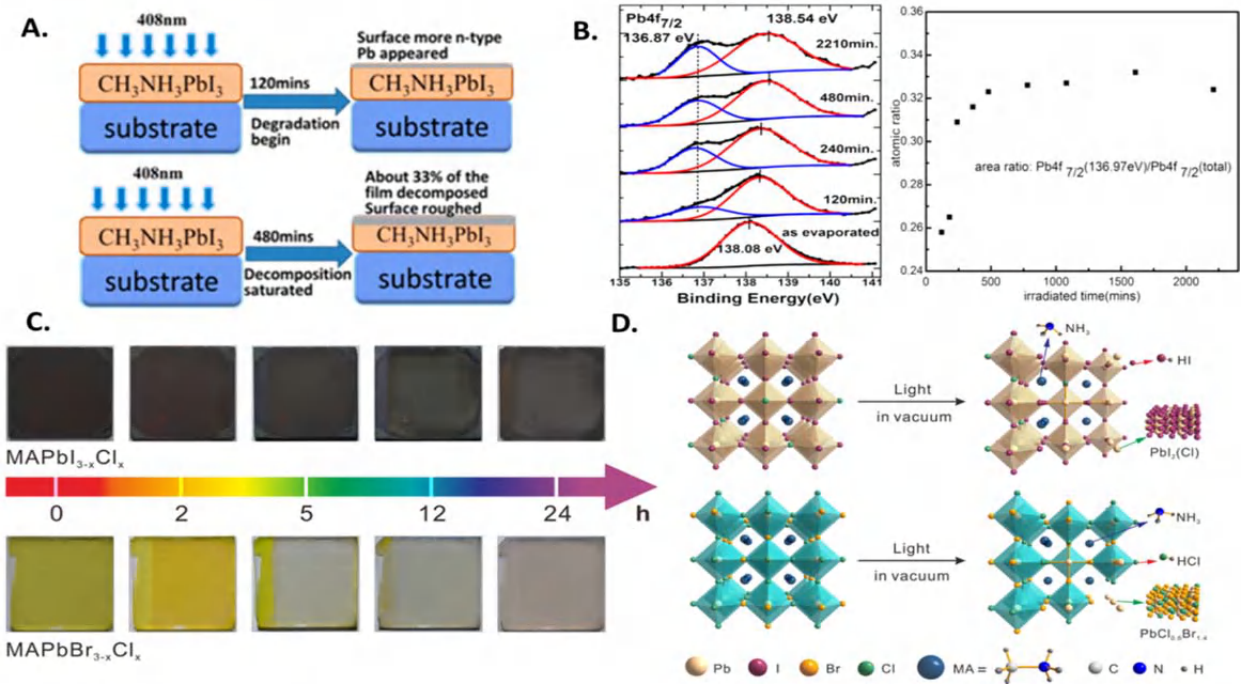

Figure 1. Light induced degradation of halide perovskite thin films: **(A)** Schematics showing the degradation of $CH_3NH_3PbI_3$, under light illumination; **(B)** XPS data on Pb 4f7/2 and metallic Pb fraction during light illumination showing the saturation of degradation; **(C)** Optical images of $MAPbI_{3-x}Cl_x$ and $MAPbBr_{3-x}Cl_x$ perovskites films with various illumination durations; **(D)** Schematics of the light-induced degradation processes for perovskite films of $MAPbI_{3-x}Cl_x$ and $MAPbBr_{3-x}Cl_x$. **(A, B)** reproduced with permission from Li *et al.*[40], Copyright (2017) American Chemical Society; **(C, D)** reproduced with permission from Xu[41], Copyright (2018) American Chemical Society.

A similar degradation also occurs for perovskite thin film with mixed halide of iodine and clorine, as well as bromine and clorine under light illumination, which was studied by Ruipeng Xu *et al* in detail: $CH_3NH_3PbI_{3-x}Cl_x$ and $CH_3NH_3PbBr_{3-x}Cl_x$ films are found to undergo degradation process as is shown by the optical images in **Figure 1C**[41]. In this degradation process, the illumination breaks the chemical bonds between CH_3NH_3 and Pb, besides, the C–N bonds in CH_3NH_3 and the CH_3NH_3 cation convert from the crystal form to hydrocarbon species, demonstrated by the schematics in **Figure 1D**[41]. Further light illumination causes different behaviour in these two mixed halide perovskite materials: in the case of $CH_3NH_3PbI_{3-x}Cl_x$, light illumination further breaks the Pb–I bonds in PbI_2 and induces the conversion of Pb^{2+}in PbI_2 into metallic Pb, and iodine sublimes into gaseous form, while such results are not observed in the case of $CH_3NH_3PbBr_{3x}–Cl_x$[41]. The above mentioned processes

can be summarized by the following chemical equations (3, 4, 5):

$$CH_3NH_3PbI_{3-x}Cl_x \xrightarrow{light} (\text{-}CH_2\text{-}) + NH_3 + HI + PbI_2(Cl) \quad (3)$$

$$PbI_2(Cl) \xrightarrow{light} Pb + I_2 + (Cl_2) \quad (4)$$

$$PbCl_{0.6}Br_{1.4} \quad (5)$$

However, different from the decrease of PL, Chen *et al*. reported light induced PL enhancement of $MAPbX_3$ thin film at low excitations and PL quenching at high excitations in well-capsulated perovskite thin film[44]. The samples are well capsulated by PMMA and glass slip, excluding the effect of moisture and oxygen, but this report raises a question why the PL changes differently in nitrogen gas and capsulated cases, which needs further investigation.

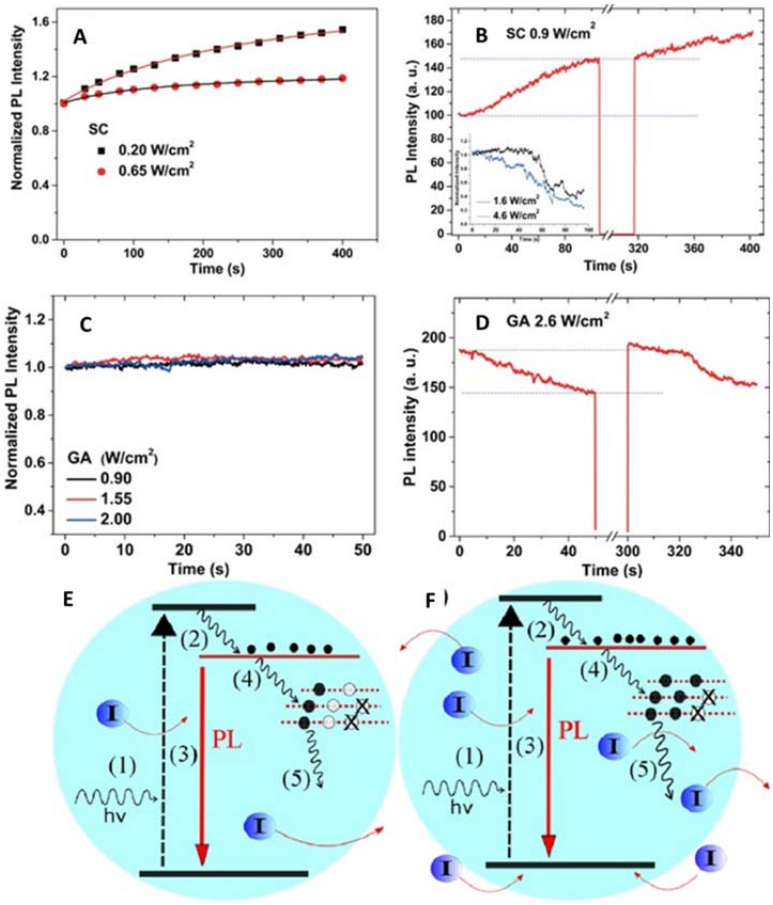

Figure 2. PL enhancement and quenching of halide perovskite thin films, reproduced with permission from Chen *et al*.[53], Copyright (2016) American Chemical Society: PL intensities of spin coating (SC) sample over time under **(A)** light excitations at 0.2 and 0.65 W/cm^2 and **(B)** light excitation at 0.9 W/cm^2, stopping at 100s for 4 minutes before resumption. PL intensities of sample fabricated by gas-assisted (GA) process over time under light excitations at **(C)** 0.90; 1.55 and 2.00 W/cm^2 and **(D)** 2.6 W/cm^2, stopping at 50s for 4 minutes before resumption. Schematics show the dynamic processes under **(E)** PL increment at low excitation; **(F)** PL quenching under high excitation. The physical processes are (1) photon excitation; (2) fast hot carrier cooling; (3) electron-hole recombination; (4) defect/surface trapping (black circle) and curing traps (cross); (5) trapped electron relaxation (detrapping) respectively.

They found the light induced effect is dependent on fabrication method. For example, the sample fabricated by convention spin coating (SC) exhibits increase in PL with light illumination, while the sample from a gas-assisted (GA) process shows a constant PL response due to a higher density of defects[44]. In detail, **Figure 2A** demonstrates that in the case of SC sample, the PL intensity increases continuously and then saturates at low excitation at 0.2 and 0.65 W/cm^2. In **Figure 2B**, the sample is firstly irradiated with laser at excitation 0.9 W/cm^2 for 100 seconds during which the PL intensity increases. Then the sample is kept in the dark for about 4 mins, and when the excitation is resumed, the PL intensity is found to remain stable. In this study, the light induced enhancement effect on the

PL of SC sample at low excitation is attributed to defect curing effect (**Figure 2E**), in which upon light illumination the defect trapping (process (4) shown by black circles in **Figure 2E**) decreases and carrier radiative recombination (process (3) in **Figure 2E**) increases, leading to increasing PL intensity in SC samples. Mosconi *et al*. reported that under illumination, Frenkel defects are annihilated[42]. In comparison, GA sample has higher density defect and the defect curing effect is trivial leading to a constant PL.

At high excitation, PL of SC samples quenches continuously and the thin film degrades, as is demonstrated in the inset of **Figure 2B**, in which the PL intensity tends to lower over time. However, PL intensity of GA sample does not change even at excitation of 2 W/cm^2 (**Figure 2C**). PL intensity of GA sample decreases with further increase of the excitation to 2.6 W/cm^2, and after being kept in dark for 4 minutes in the dark, PL intensity of GA sample changes back to its initial level (**Figure 2D**). Note that with respect to the original PL intensity, the PL at a time of 10s and at power of 4.6 W/cm^2 (46 J/cm^2) decreases, while PL at a time of 230s and at power of 0.2W/cm^2 is higher, suggesting that the excitation power is a critical parameter in determining the light induced PL changes of perovskites. The PL intensities for both samples quench under high excitations, and this results from mobile ion accumulation and increased non-radiative electron/hole recombination, as is shown in **Figure 2F**[53]. At high excitation, mobile ions can be activated probably via activation of pre-existing ions or via decomposition of the perovskite by the high density of photo-carriers. Then the ions migrate and accumulate at the grain boundary or interfaces, leading to enhanced non-radiative recombination of free carriers and consequently PL quenching[44].

2.2 In the presence of O_2 or/and moisture

As one would expect, the degradation process is more complicated when the LHPs are in the presence of oxygen. As **Table 2** demonstrates, literatures reported that in the presence of light and oxygen, for the thin films, at low excitation power and dose (power of 0.188 to 0.5 W/cm^2, dose of 33 to 150 J/cm^2), the PL enhancement is found, while decomposition is observed at higher excitation power or dose.

Table 2. The literatures of light illumination on halide perovskite in presence of O_2 or/and moisture

Material	Light illumination	Environment	Film morphology	PL	Ref
$MAPbI_3$ film	405 nm laser, 0.5 W/cm^2 for 5 mins (150 J/cm^2)	Oxygen or moisture		Continuous enhancement	[52]
$MAPbI_3$ film	532 nm, 0.188 W/cm^2 for 3 mins (33.8 J/cm^2)			Continuous enhancement	[54]
$MAPbI_3$ film	Tungsten halogen lamp (broadband), 1.5 W/cm^2 for up to 3 days (388 J/cm^2)	Oxygen	Decomposition	Not reported	[55]
$MAPbI_3$ film	<425 nm Edmund Optics, 0.1 W/cm^2 for up to 2 days (17200 J/cm^2)	Moisture	Decomposition	Not reported	[39]
$MAPbI_3$ nanocrystals	514 nm (an Argon ion laser), 10 W/cm^2 for seconds (100J/cm^2)	Air (oxygen and moisture)	Decomposition	PL intensity decreases, Blue shift	[56]

The underlying mechanism of PL enhancement is as follows: Oxygen diffuses into the films rapidly, and under light excitation of $MAPbI_3$, photoinduced electrons and holes form $MAPbI_3$*, which then transfers the electron to O_2 and produces superoxide species. Moreover, iodide vacancies are found to be the preferential sites in leading to photo-induced formation of these superoxide species from O_2[55]. This consequently removes electron trap states associated with the iodide vacancies, leading to PL enhancement of the perovskite films, as is reported by Roberto Brenes *et al*. very recently[52].

The perovskite thin film shows heterogeneous PL comprised of defect-rich dark domains and bright domains that are less defective, because of the heterogeneous distribution of trap states from grain to grain, as is shown in **Figure 3A**, **B**. Dane *et al*. conducted a detailed micro-scale study and illustrated that despite of the overall bulk PL enhancement of the films, the extent of PL enhancement varies from grain to grain. The authors found that under light illumination, dark regions with higher

trap state densities are preferentially brightened due to reduction of trap states and a redistribution in local emission intensities is also induced (**Figure 3C** shows the variation of the local emission of different spots over time)[54]. The emission of bright spot (red triangle in **Figure 3B**) only increases by a factor of 1.4, while the dark spot (blue circle in **Figure 3B**) increases by a factor of 8.7 after ~3 min of illumination. Very importantly, they also observed that reduction in the trap density is accompanied by photo-induced iodine migration: A dark spot is illuminated for several minutes with pulsed excitation (1.2 kJ cm^{-2}) and photoluminescence decay is recorded (**Figure 3D**). Iodide distribution summed through the depth in the illuminated region is shown in **Figure 3E**. The iodide distribution (columns) and laser intensity (blue curve) across the line scan (blue arrow in **Figure 3E**) in **Figure 3F** shows that the regions of highest illumination intensity have least iodide, while the adjacent regions have higher level of iodide compared to the background iodide levels, indicating migration of iodine from the illumination area to adjacent areas.

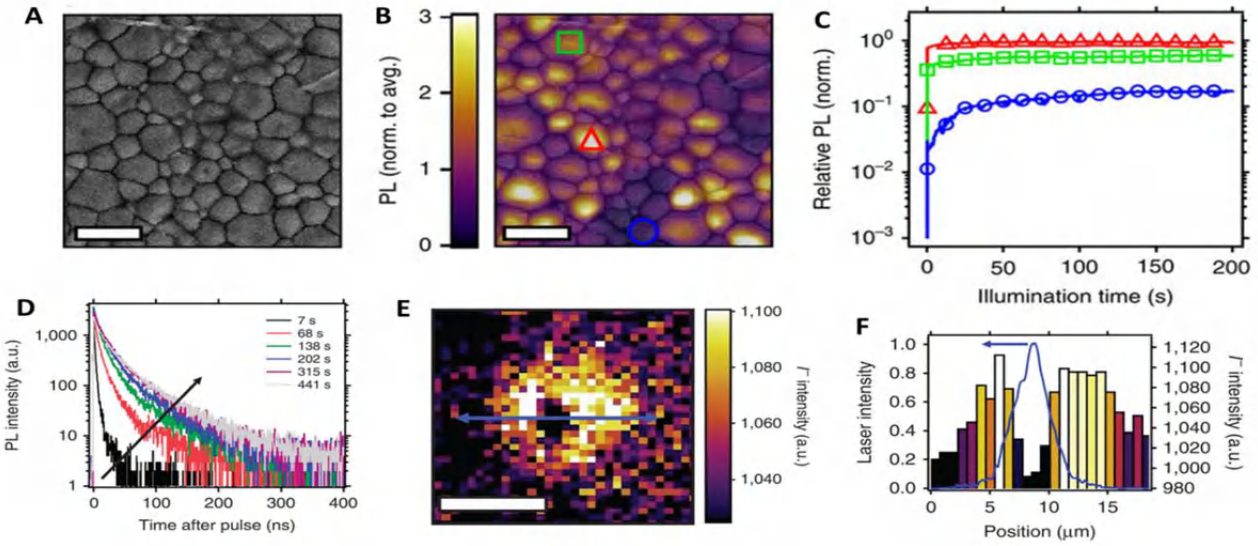

Figure 3. Microscale study of light induced PL changes of halide perovskite thin films, reproduced with permission from Dequilettes *et al.*[54], Copyright (2016) Nature Publishing Group; **(A)** Correlated scanning electron microscopy (SEM) image; and **(B)** PL image of a perovskite film measured in nitrogen with semitransparent SEM image overlaid, scale bars, 2 μm; **(C)** PL intensity over time from a dark spot (blue circles, enhancement of 8.7 times), intermediate spot (green squares, enhancement of 1.6 times) and a bright spot (red triangles, enhancement of 1.4 times) corresponding to the regions highlighted with the same symbols in **(B)**; **(D)** A series of time-resolved PL decays from a $CH_3NH_3PbI_3$ film measured over time under illumination before time-of-flight secondary-ion-mass spectrometry (ToF-SIMS) measurements; **(E)** ToF-SIMS image of the iodide (I^-) distribution summed through the film depth, scale bar, 10 μm; **(F)** Line scan of the blue arrow in **(E)** to show the iodide distribution (right axis). The measured spatial profile of the illumination laser (blue) is shown on the left axis**.**

Decomposition is also found to occur at high excitations, because the superoxide species is highly reactive and reacts with $MAPbI_3$. After reaction, $MAPbI_3$ is decomposed into methylamine, PbI_2, and I_2 through the equation (6, 7, 8) below[25,55].

$$MAPbI_3 \xrightarrow{\text{Light No moisture}} MAPbI_3^* \quad (6)$$

$$O_2 \xrightarrow{MAPbI_3^*} MAPbI_3 + O_2^- \quad (7)$$

$$\xrightarrow{\text{Deprotonation}} MeNH_2 + PbI_2 + 1/2I_2 + H_2O \quad (8)$$

The degradation in light soaking and oxygen can be reduced with several methods: production of perovskite films with large crystallites to produce less photo-induced superoxide[55], and passivation of the perovskite films with iodide salts[55].

At low excitation in the presence of moisture, under light illumination, PL is enhanced probably due to formation of a shell on the surfaces which converts the surfaces to species, which does not deteriorate the PL[52]. It is generally agreed till now that moisture alone induces hydration of $CH_3NH_3PbI_3$ films is a reversible process[31,32,57], while light illumination with high excitations in the presence of moisture induces irreversible degradation of perovskite and forms PbI_2, as is reported by Ahn *et al.*[39]. They reveal the mechanism of degradation of perovskite thin film under light illumination in the presence of moisture as follows: trapped charges are generated along the grain boundaries by light excitation, which induce local electric field, distort the structure of hydrated perovskite and trigger the ir-

reversible humidity-induced degradation of perovskite[39]. **Figure 4A** shows that in the dark condition with relative humidity (RH) 90% $MAPbI_3$ is hydrated after two days and can be dehydrated reversibly by nitrogen gas drying. However, it shows very fast irreversible degradation under light soaking even at lower RH 20% (see **Figure 4B**).

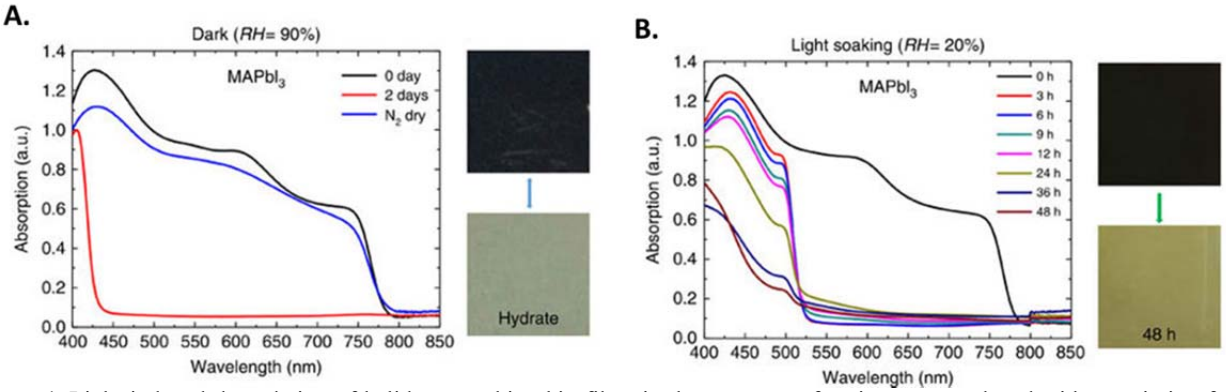

Figure 4. Light induced degradation of halide perovskite thin films in the presence of moisture, reproduced with permission from Ahn *et al.*[39], Copyright (2016) Nature Publishing Group; **(A)** Absorption spectra and pictures of the $MAPbI_3$ perovskite film and the optical images before and after ageing for two days under dark conditions at 90% RH showing that $MAPbI_3$ perovskites were transformed into transparent hydrated states after two days; **(B)** Time evolution of absorption spectra and pictures of $MAPbI_3$ before and after degradation at 20% RH under simultaneous light soaking.

In a layered geometry (thin film) the light-induced decomposition occurs at high excitations and is only on the surface, and therefore shows no spectral shift. While for the nanocrystals, the surface is high and therefore the decomposition occurs at lower excitations, and leads to clear spectra shift, shown in the last row of **Table 2**. For instance, when the solution of perovskite is spin-coated with low concentration, crystals form instead of a continuous film. Under intense light excitation, a local field gradient is induced in $MAPbI_3$ crystals, inducing migration of methylammonium ions (MA^+) which distorts the lattice structure and changes the effective band gap. The three-dimensional $MAPbI_3$ crystal structure collapses to the two-dimensional layered PbI_2 structure, as shown in **Figure 5**. The dis-tortion of the Pb–I–Pb angle caused by an increasing number of defects (ionic vacancies) lead to spectrally shifting PL[56]. It is worth noting that the effect of light illumination on PL of perovskite thin film is similar in the case of capsulated film and in the presence of oxygen or moisture. Therefore, one would need further confirmation whether the oxygen and moisture is eliminated completely in a capsulated film.

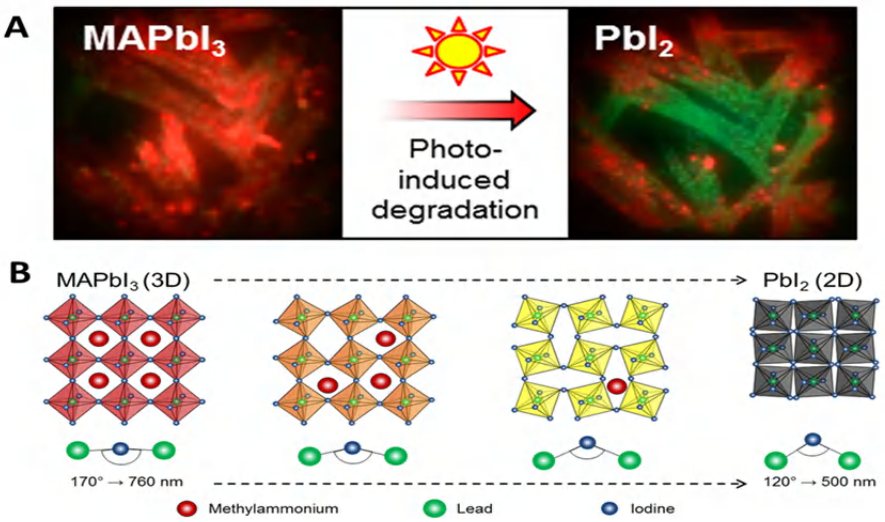

Figure 5. Light induced PL spectral shift of $MAPbI_3$ nanocrystals in ambient, reproduced with permission from ref.[56], Copyright (2016) American Chemical Society: **(A)** PL image before the degradation of a $MAPbI_3$ bulk sample and after the degradation. **(B)** Schematic showing structural change.

2.3 Light induced segregation of (MA)Pb(BrxI1-x)3 thin film

In a tandem configuration with a bottom cell with a lower bandgap (Si), perovskite material with a high bandgap of 1.7–1.8 eV is needed for the top cell. Mixed halide perovskite (MA)Pb(Br_xI_{1-x})$_3$ satisfies this requirement, however, when the excitation intensity is above a threshold, light induced reversible phase segregation occurs: upon illumination bromide and iodide ions phase segregate into Br-rich and I-rich domains with lower bandgap acting as traps and limiting the performance of solar cells[45-50].

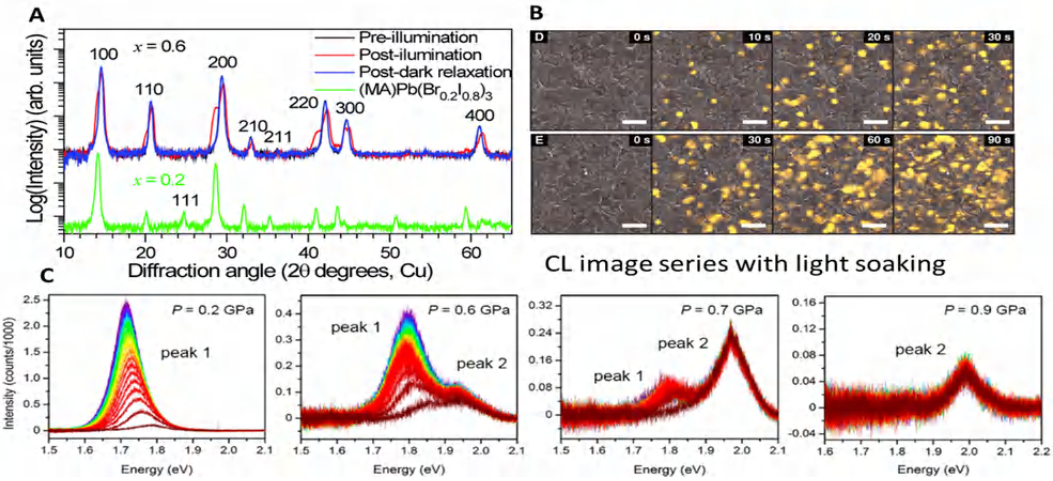

Figure 6. Light induced phase segregation in (MA)Pb(Br_xI_{1-x})$_3$ thin film: **(A)** XRD pattern of a (MA)Pb(Br_xI_{1-x})$_3$ (x = 0.6) film before (black) and after (red) white-light soaking for 5 minutes at ~50 mW cm^{-2}, and after 2 h in the dark (blue), reproduced with permission from Slotcavage *et al.*[45], Copyright (2016) American Chemical Society; **(B)** CL image series with (D) 10 and (E) 30 s of light soaking between each CL image. The scale bars are 2 μm, reproduced with permission from Bischa *et al.*[49], Copyright (2017) American Chemical Society; **(C)** PL spectra recorded Spectra displayed were obtained at 0.2 GPa, 0.6 GPa, 0.7 GPa, and 0.9 GPa, at 8 s intervals for (MA)Pb($Br_{0.6}I_{0.4}$)$_3$ showing the PL evolution with light soaking, ranging from 0 s (dark red) to 150 s (purple), reproduced with permission from Jaffe *et al.*[59], Copyright (2016) American Chemical Society.

This is evidenced by multiple experimental observations in the literatures, including XRD, PL and cathodoluminescence, and transient absorption measurements. When illuminated with white light, the original XRD pattern of (MA)Pb(Br_xI_{1-x})$_3$ thin film split into two peaks, indicating phases of two types of domains, which reverses to one peak when the sample is back to dark condition, as is shown in **Figure 6A**[45]. The ion segregation occurs through the halide defects and the I-rich domains locate at the grain boundaries in the thin film, as is demonstrated in **Figure 6B**[49]. Therefore, the segregation can be reduced by improving the crystallinity and producing larger grain sizes. The other way to minimize the segregation is through compositional tuning or compressing of the perovskite material. Bischak *et al.* suggest that by replacing MA with formamidinium (FA) or Cs the light induced segregation can be reduced, and also experimentally phase stability was reported for Cs and Cs/FA blends[49,58]. Besides, applying high pressure could also alleviate the segregation phenomenon by thermodynamically or kinetically suppress halide migration[59]. As is shown in **Figure 6C**, at a pressure of 0.9 GPa, the perovskite shows no PL red shift since light induced phase segregation is inhibited in the high-pressure phase.

3. Conclusions

In conclusion, the interaction of light and perovskite involves many physical processes depending on the environment (vacuum, nitrogen, capsulated by other layers, oxygen, moisture), light illumination conditions (excitation power, dose), and the morphology of samples (thin film or nanocrystal, the grain size of the thin film). The enhancement of PL induced by light illumination occurs at low excitations and several possible pathways reported so far can be summarized as follows: defect curing in a capsulated film; reduction of iodine vacancies associated electron traps by reaction of oxygen, photoinduced electron and hole and perovskite when

exposed to oxygen, formation of a shell by moisture to inhibit PL quenching when exposed to moisture. The quenching of PL takes place at higher light illumination, and the underlying mechanism is either by inducing defects in the case of nitrogen or vacuum, or through mobile ion accumulation and increased non-radiative electron/hole recombination in a capsulated film. At high excitations, the perovskite is also found to be decomposed into PbI_2 in the following cases: in vacuum, the volatile products desorb instantly; in an oxygen atmosphere, the reactive superoxide species are formed and decompose perovskite efficiently; in a humid environment, light generates trapped charges along the grain boundaries, which triggers the irreversible humidity-induced degradation of perovskite. Besides, in Br/I mixed halide perovskite thin film, light induces ion segregation through halide defects and the film segregates into iodine domains and bromine domains, which reverse back to the mixed halide perovskite in the dark conditions. The summary encourages us with the conclusion that the light illumination is not always detrimental for perovskite materials, and instead can be utilized to enhance the optical properties in the proper configurations and to improve the performances of perovskite-based devices. Despite the above conclusions, several points still need to be addressed such as the reason that at low excitations, PL decreases in a nitrogen atmosphere but increases in a capsulated film, in the case of PL enhancement in oxygen atmosphere at low excitations whether any morphological or compositional changes occur.

Author Contributions

Z. Y. D proposed to review, and D. A. D commented and corrected the work.

Conflict of Interest

No conflict of interest was reported by the authors.

Acknowledgement

Zhiya Dang acknowledges funding from the European Union under grant agreement No. 614897 (ERC Grant TRANS-NANO).

References

1. Pellet N, Peng G, Gregori G, *et al.* Mixed-organic-cation perovskite photovoltaics for enhanced solar-light harvesting. Angewandte Chemie International Edition 2014; 53(12): 3151–3157.
2. Eperon GE, Stranks SD, Menelaou C, *et al*. Formamidinium lead trihalide: A broadly tunable perovskite for efficient planar heterojunction solar cells. Energy & Environmental Science 2014; 7(3): 982–988.
3. Stranks SD, Snaith HJ. Metal-halide perovskites for photovoltaic and light-emitting devices. Nature Nanotechnology 2015; 10(5): 391–402.
4. Beal RE, Slotcavage DJ, Leijtens T, *et al*. Cesium lead halide perovskites with improved stability for tandem solar cells. Journal of Physical Chemistry Letters 2016; 7(5): 746–751.
5. Sjoerd A, Veldhuis, Pablo P, *et al*. Perovskite materials for light-emitting diodes and lasers. Advanced Materials 2016; 28(32): 6804–34.
6. Sum TC. Halide Perovskite Lasers. CLEO: Conference on Lasers and Electro-Optics; 2017.
7. Ahmadi M, Wu T, Hu B. A review on organic–inorganic halide perovskite photodetectors: Device engineering and fundamental physics. Advanced Materials 2017; 29(41): 1–24.
8. Wangyang P, Gong C, Rao G, *et al*. Recent advances in halide perovskite photodetectors based on different dimensional materials. Advanced Optical Materials 2018; 6(11): 1–30.
9 Dang Y, Ju D, Wang L, *et al*. Recent progress in the synthesis of hybrid halide perovskite single crystals. CrystEngComm 2016; 18(24): 4476–4484.
10. Bai S, Yuan Z, Gao F. Colloidal metal halide perovskite nanocrystals: synthesis, characterization, and applications. Journal of Materials Chemistry C 2016; 4(18): 3898–3904.
11. Yang Z, Zhang S, Li L, *et al*. Research progresses on large-area perovskite thin films and solar modules. Journal of Materiomics 2017; 3(4): 231–244.
12. Miyata A, Mitioglu A, Plochocka P, *et al*. Direct measurement of the exciton binding energy and effective masses for charge carriers in organic-inorganic tri-halide perovskites. Nature Physics 2015; 11(7): 582–587.
13. Protesescu L, Yakunin S, Bodnarchuk MI, *et al*. Nanocrystals of cesium lead halide perovskites (CsPbX3, X = Cl, Br, and I): Novel optoelectronic materials showing bright emission with wide color gamut. Nano Letters 2015; 15(6): 3692–3696.
14. Shi D, Adinolfi V, Comin R, *et al*. Low trap-state density and long carrier diffusion in organolead trihalide perovskite single crystals. Science 2015; 347 (6221): 519–522.
15. Unger EL, Kegelmann L, Suchan K, *et al*. Roadmap and roadblocks for the band gap tunability of metal halide perovskites. Journal of Materials Chemistry A 2017; 5(23): 11401–11409.
16. Liu H, Wu Z, Shao J, *et al*. $CsPb_xMn_{1-x}Cl_3$ perovskite quantum dots with high Mn substitution ratio.

ACS Nano 2017; 11(2): 2239–2247.
17. Jellicoe TC, Richter JM, Glass HFJ, *et al*. Synthesis and optical properties of lead-free cesium tin halide perovskite nanocrystals. Journal of the American Chemical Society 2016; 138(9): 2941–2944.
18. Zhang J, Yang Y, Deng H, *et al*. High quantum yield blue emission from lead free inorganic antimony halide perovskite colloidal quantum dots. ACS Nano 2017; 11(9): 9294–9302.
19. Leng M, Chen Z, Yang Y, *et al*. Lead-free, blue emitting bismuth halide perovskite quantum dots. Angewandte Chemie-International Edition 2016; 55 (48): 15012–15016.
20. Creutz SE, Siena MCD, Creutz SE, *et al*. Colloidal nanocrystals of lead-free double-perovskite (elpasolite) semiconductors: Synthesis and anion exchange to access new materials. Nano Letters; 2018; 18(2): 1118–1123.
21. Zhang L, Ju M, Liang W. The effect of moisture on the structures and properties of lead halide perovskites: A first-principles theoretical investigation. Physical Chemistry Chemical Physics 2016; 18(33): 23174–23183.
22. Ma H, Imran M, Dang Z, *et al*. Growth of metal halide perovskite, from nanocrystal to micron-scale crystal: A review. Crystals 2018; 8(5): 182.
23. Conings B, Drijkoningen J, Gauquelin N, *et al*. Intrinsic thermal instability of methylammonium lead trihalide perovskite. Advanced Energy Materials 2015; 5(15): 1–8.
24. Yang J, Siempelkamp BD, Liu D, *et al*. Investigation of $CH_3NH_3PbI_3$ degradation rates and mechanisms in controlled humidity environments using in situ techniques. ACS Nano 2015; 9(2): 1955–1963.
25. Aristidou N, Sanchez-Molina I, Chotchuangchutchaval T, *et al*. The role of oxygen in the degradation of methylammonium lead trihalide perovskite photoactive layers. Angewandte Chemie-International Edition 2015; 54(28): 8208–8212.
26. Manser JS, Saidaminov MI, Christians JA, *et al*. Making and breaking of lead halide perovskites. Accounts of Chemical Research 2016; 49(2): 330–338.
27. Dang Z, Shamsi J, Palazon F, *et al*. In situ transmission electron microscopy study of electron beam-induced transformations in colloidal cesium lead halide perovskite nanocrystals. ACS Nano 2017; 11(2): 2124–2132.
28. Dang Z, Shamsi J, Akkerman QA, *et al*. Low-temperature electron beam-induced transformations of cesium lead halide perovskite nanocrystals. ACS Omega 2017; 2(9): 5660–5665.
29. Philippe B, Park BW , Lindblad R, *et al*. Chemical and electronic structure characterization of lead halide perovskites and stability behavior under different exposures — A photoelectron spectroscopy investigation. Chemistry of Materials 2015; 27(5): 1720–1731.
30. Han Y, Meyer S, Dkhissi Y, *et al*. Degradation observations of encapsulated planar $CH_3NH_3PbI_3$ perovskite solar cells at high temperatures and humidity. Journal of Materials Chemistry A 2015; 3(15): 8139–8147.
31 Leguy AMA, Hu Y, Campoy-Quiles M, *et al*. Reversible hydration of $CH_3NH_3PbI_3$ in films, single crystals, and solar cells. Chemistry of Materials 2015; 27(9): 3397–3407.
32. Christians JA, Herrera PAM, Kamat PV. Transformation of the excited state and photovoltaic efficiency of $CH_3NH_3PbI_3$ perovskite upon controlled exposure to humidified air. Journal of the American Chemical Society 2015; 137(4): 1530–1538.
33. Brunetti B, Cavallo C, Ciccioli A, *et al*. On the thermal and thermodynamic (in)stability of methylammonium lead halide perovskites. Scientific Reports 2016; 6: 1–10.
34. Huang W, Sadhu S, Ptasinska S. Heat- and gas-induced transformation in $CH_3NH_3PbI_3$ perovskites and its effect on the efficiency of solar cells. Chemistry of Materials 2017; 29(19): 8478–8485.
35. Milosavljević AR, Huang W, Sadhu S, *et al*. Low-energy electron-induced transformations in organolead halide perovskite. Angewandte Chemie International Edition 2016; 55(34): 10083–10087.
36. Yu Y, Zhang D, Kisielowski C, *et al*. Atomic resolution imaging of halide perovskites. Nano Letters 2016; 16(12): 7530–7535.
37. Wang Y, Li X, Sreejith S, *et al*. Photon driven transformation of cesium lead halide perovskites from few-monolayer nanoplatelets to bulk phase. Advanced Materials 2016; 28(48): 10637–10643.
38. Yuan H, Debroye E, Janssen K, *et al*. Degradation of methylammonium lead iodide perovskite structures through light and electron beam driven ion migration. The Journal of Physical Chemistry Letters 2016; 7(3): 561–566.
39. Ahn N, Kwak K, Jang SM, *et al*. Trapped charge-driven degradation of perovskite solar cells. Nature Communications 2016; 7: 1–9.
40. Li Y, Xu X, Wang C, *et al*. Light-induced degradation of $CH_3NH_3PbI_3$ hybrid perovskite thin film. Joornal of Physical Chemistry C 2017; 121(7): 3904–3910.
41. Xu R, Li Y, Jin T, *et al*. In situ observation of light illumination-induced degradation in organometal mixed-halide perovskite films. Acs Applied Materials & Interfaces 2018; 10(7): 6737–6746.
42. Mosconi E, Meggiolaro D, Snaith HJ, *et al*. Light-induced annihilation of frenkel defects in organolead halide perovskites. Energy & Environmental Science 2016; 9(10): 3180–3187.
43. Li C, Zhong Y, Luna C A, *et al*. Emission enhancement and intermittency in polycrystalline organolead halide perovskite films. Molecules 2016; 21(8): 1081.
44. Chen S, Wen X, Huang S, *et al*. Light illumination induced photoluminescence enhancement and quenching in lead halide perovskite. Solar Rrl 2017; 1 (1).
45. Slotcavage DJ, Karunadasa HI, McGehee MD. Light-induced phase segregation in halide-perovskite absorbers. ACS Energy Letters 2016; 1(6): 1199–

1205.
46. Li W, Rothmann MU, Liu A, *et al*. Phase segregation enhanced ion movement in efficient inorganic $CsPbIBr_2$ solar cells. Advanced Energy Material 2017; 7(20): 1–13.
47. Yoon SJ, Draguta S, Manser JS, *et al*. Tracking iodide and bromide ion segregation in mixed halide lead perovskites during photoirradiation. ACS Energy Letters 2016; 1(1): 290–296.
48. Barker AJ, Sadhanala A, Deschler F, *et al*. Defect-assisted photoinduced halide segregation in mixed-halide perovskite thin films. ACS Energy Letters 2017; 2(6): 1416–1424.
49. Bischak CG, Hetherington CL, Wu H, *et al*. Origin of reversible photoinduced phase separation in hybrid perovskites. Nano Letters 2017; 17(2): 1028–1033.
50. Hoke ET, Slotcavage DJ, Dohner ER, *et al*. Rever sible photo-induced trap formation in mixed-halide hybrid perovskites for photovoltaics. Chemical Science 2015; 6(1): 613–617.
51. Brivio F, Caetano C, Walsh A. Thermodynamic origin of photoinstability in the $CH_3NH_3Pb(I_{1-x}Brx)_3$ hybrid halide perovskite alloy. Journal of Physical Chemistry Letters 2016; 7(6): 1083–1087.
52. Brenes R, Eames C, Bulović V, *et al*. The impact of atmosphere on the local luminescence properties of metal halide perovskite grains. Advanced Materials 2018; 30(15): 1–8.
53. Chen S, Wen X, Sheng R, *et al*. Mobile ion induced slow carrier dynamics in organic-inorganic perovskite $CH_3NH_3PbBr_3$. ACS Applied Materials & Interfaces 2016; 8(8): 5351–5357.
54. Dequilettes DW, Zhang W, Burlakov VM, *et al*. Photo-induced halide redistribution in organic-inorganic perovskite films. Nature Communications 2016; 7: 1–9.
55. Aristidou N, Eames C, Sanchez-Molina I, *et al*. Fast oxygen diffusion and iodide defects mediate oxygen-induced degradation of perovskite solar cells. Nature Communications 2017; 8: 1–10.
56. Merdasa A, Bag M, Tian Y, *et al*. Super-resolution luminescence microspectroscopy reveals the mechanism of photoinduced degradation in $CH_3NH_3PbI_3$ perovskite nanocrystals. Journal of Physical Chemistry C 2016; 120(19): 10711–10719.
57. Habisreutinger SN, Leijtens T, Eperon GE, *et al*. Carbon nanotube/polymer composites as a highly stable hole collection layer in perovskite solar cells. Nano Letters 2014; 14(10): 5561–5568.
58. McMeekin DP, Sadoughi G, Rehman W, *et al*. A mixed-cation lead mixed-halide perovskite absorber for tandem solar cells. Science 2016; 351(6269): 151–155.
59. Jaffe A, Lin Y, Beavers CM, *et al*. High-pressure single-crystal structures of 3D lead-halide hybrid perovskites and pressure effects on their electronic and optical properties. ACS Central Science 2016; 2(4): 201–209.

Peer Review Process

All manuscripts are subjected to a stringent peer review process. This is to uphold the high quality of papers published in this journal and ensure that the reporting of research work is truthful and precise.

1. All submitted manuscript are firstly handled by our managing editor, who will check the manuscript for plagiarism, in which rejection of the manuscript can take place at this stage by the managing editor if plagiarism occurs in the manuscript.

2. After the plagiarism check is completed and results are deemed satisfactory, the managing editor will pass the manuscript to the Editor-in-Chief who will undertake the peer review process, or at times pass the task to one of the Associate Editors.

3. A minimum of 2 reviewers will be selected from the pool of reviewers available according to their expertise and suitability to the subject matter of the manuscript. Reviewers will have to give their comments and recommendations (**Accept, Revisions Required, Resubmit for Review or Reject**) to the Editor-in-Chief or Associate Editor for them to make a final decision on the paper, and their comments will help the authors improve their papers.

4. Upon recommendations by the reviewers, the Editor-in-Chief or the Associate Editor can make a final decision on the paper and inform the author on their decision, adding comments to the Authors to make improvements in their research or paper.

    - If the decision is to **Accept Submission** (no amendments required by author), the manuscript will be sent to the Editing stage.
    - If Editor-in-Chief suggests **Revisions Required** (minor revisions), authors are given a maximum of 2 weeks to revise and resubmit the article.
    - If Editor-in-Chief suggests **Resubmit for Review** (major revisions), authors are given a maximum of 4 weeks to revise and resubmit the article for the second round of review.
    - If the decision is to **Reject Submission**, the author will be notified and the rejected manuscript will be archived and the peer review process ends.

5. An accepted paper will be sent for Copy Editing, Layout Editing and Proofreading before publication. Correspondence between the authors and editors will be required here in order to improve the language and/or look of the manuscript. After the Editing stage is completed, authors are required to check the PDF file of the final version before the article is published. EnPress Publisher registers DOI for the manuscript after publication, in which the article is immediately accessible to the public.

6. Authors may appeal for a rejected submission. Appeal requests must be made in writing to contact@enpress-publisher.com with detailed reasons for the appeal and point by point responses to the reviewers' remarks. Decisions on appeals are final and no further consideration will be made.

Characterization and Application of Nanomaterials

Focus and Scope

Characterization and Application of Nanomaterials is an international open access journal that publishes original research articles and review articles related to all areas of nanomaterials.

This journal covers modeling, simulation, nanotechnology, thin film, fabrication, synthesis and properties of nanomaterials.

EnPress Publisher, LLC

EnPress Publisher, LLC, is a scholastic conduit for an assembly of professionals in the domains of science, technology, medicine, engineering, education, social sciences and many more, as a roundtable for their intellectual discourse and presentation, and as an instrument to galvanize research designs, policy implementation and commercial interests, to facilitate the prevailing over their challenges and to encourage to the full advantage of their resources and true potential.

We are the intellectual and academic home for academic, educators, scholars, clinicians, corporate researchers, who all play important roles in a wide range of national and international research organisations, and whose interests, expertise, research approaches and industry objectives from around the world coalesce together to advance significant contributions in their research and professional fields.

As an instrument of information purveyor, we seek to combine academic rigor and originality with the nuanced development of policy and practice. Via our journals, client database, online campaigns and social media presence, we offer a platform for industry professionals to interconnect, as well as opening doors towards cost-effective solutions for them to succeed, and we confidently hope to inspire a new generation of multidisciplinary researchers, think-tank experts, policymakers and business entities to innovate and advance their knowledge across fields.

EnPress Publisher,LLC

Add 14701 Myford Road,Suite B-1,Tustin,CA 92780,United States

Tel +1（949）299 0192

Emali contact@enpress-publisher.com

Web https://enpress-publisher.com